

1 **Low Cobalt Inventories in the Amundsen and Ross Seas Driven by High Demand for**  
2 **Labile Cobalt Uptake Among Native Phytoplankton Communities**

3 **Rebecca J. Chmiel<sup>1,2</sup>, Riss M. Kellogg<sup>1,2</sup>, Deepa Rao<sup>1,2</sup>, Dawn M. Moran<sup>2</sup>, Giacomo R.**  
4 **DiTullio<sup>3</sup>, and Mak A. Saito<sup>2</sup>**

5 <sup>1</sup> MIT/WHOI Joint Program in Oceanography/Applied Ocean Science and Engineering, Woods  
6 Hole, MA, 02543, USA

7 <sup>2</sup> Department of Marine Chemistry and Geochemistry, Woods Hole Oceanographic Institution,  
8 Woods Hole, MA, 02543, USA

9 <sup>3</sup> Hollings Marine Laboratory, 331 Fort Johnson, Charleston SC, 29412, USA

10

11 Corresponding author: Mak Saito ([msaito@whoi.edu](mailto:msaito@whoi.edu))

12 **Key Points:**

- 13 • A significantly smaller dCo inventory was observed in the Ross Sea during the  
14 2017/2018 austral summer compared to two expeditions in 2005/2006.
- 15 • The drawdown of the labile dCo fraction can be explained by higher rates of Co uptake  
16 by phytoplankton.
- 17 • This change may be due to the alleviation of Fe limitation through inputs from increased  
18 glacial melting and subsequent development of intermittent vitamin B<sub>12</sub> and/or Zn  
19 limitation, both of which would be expected to increase the demand for Co among  
20 plankton communities.

## 21 **Abstract**

22 Cobalt (Co) is a scarce but essential micronutrient for marine plankton in the Southern Ocean and  
23 coastal Antarctic seas where dissolved cobalt (dCo) concentrations can be extremely low. This  
24 study presents total dCo and labile dCo distributions measured via shipboard voltammetry in the  
25 Amundsen Sea, Ross Sea and Terra Nova Bay during the CICLOPS (Cobalamin and Iron Co-  
26 Limitation of Phytoplankton Species) expedition. A significantly smaller dCo inventory was  
27 observed during the 2017/2018 CICLOPS expedition compared to two 2005/2006 expeditions to  
28 the Ross Sea conducted over a decade earlier. The dCo inventory loss (~10–20 pM) was present  
29 in both the surface and deep ocean and was attributed to the loss of labile dCo, resulting in the  
30 near-complete complexation of dCo by strong ligands in the photic zone. A changing dCo  
31 inventory in Antarctic coastal seas could be driven by the alleviation of iron (Fe) limitation in  
32 coastal areas where the flux of Fe-rich sediments from melting ice shelves and deep sediment  
33 resuspension may have shifted the region towards vitamin B<sub>12</sub> and/or zinc (Zn) limitation, both of  
34 which are likely to increase the demand for Co among marine plankton. High demand for Zn by  
35 phytoplankton can result in increased Co and cadmium (Cd) uptake because these metals often  
36 share the same metal uptake transporters. This study compared the magnitudes and ratios of Zn,  
37 Cd and Co uptake ( $\rho$ ) across upper ocean profiles and observed order of magnitude uptake trends  
38 ( $\rho\text{Zn} > \rho\text{Cd} > \rho\text{Co}$ ) that paralleled the trace metal concentrations in seawater. High rates of Co and  
39 Zn uptake were observed throughout the region, and the speciation of available Co and Zn  
40 appeared to influence trends in dissolved metal : phosphate stoichiometry and uptake rates over  
41 depth. Multi-year loss of the dCo inventory throughout the water column may be explained by an  
42 increase in Co uptake into particulate organic matter ~~(POM)~~ and subsequently increased flux of  
43 Co into sediments via sinking and burial. This perturbation of the Southern Ocean Co  
44 biogeochemical cycle could signal changes in the nutrient limitation regimes, phytoplankton  
45 bloom composition, and carbon sequestration sink of the Southern Ocean.

## 46 **Plain Language Summary**

47 Cobalt is an important micronutrient for plankton, yet is often scarce throughout the oceans. A  
48 2017/2018 expedition to coastal Antarctica, including regions of the Amundsen Sea and the Ross  
49 Sea, discovered lower concentrations of cobalt compared to two past expeditions in 2005 and 2006.  
50 In particular, this expedition observed lower concentrations of deep-ocean labile cobalt, or “free”  
51 cobalt unbound to strong organic molecules, the type of cobalt preferred by phytoplankton for  
52 uptake as a micronutrient. It is possible that a shifting nutrient landscape due to changing inputs  
53 of other micronutrients like dissolved iron is causing the lower dissolved cobalt concentrations,  
54 and may also be affecting the demand for micronutrients like dissolved zinc and vitamin B<sub>12</sub>, which  
55 contains a cobalt atom. We have modeled how increased cobalt uptake by plankton can result in  
56 the lower deep cobalt concentrations over a time period of 12 years.

## 57 **1 Introduction**

58 Coastal Antarctic seas are highly productive environments for phytoplankton blooms and  
59 are characterized by high nutrient, low chlorophyll (HNLC) surface waters that tend to be growth  
60 limited by iron (Fe) and other trace metal micronutrients (Martin et al., 1990; Arrigo et al., 2008,  
61 2012). During the spring and summer months, katabatic winds and fragmenting sea ice form open  
62 coastal polynyas in the Amundsen and Ross Seas that host high phytoplankton productivity and  
63 act as significant global carbon sinks (Arrigo et al., 2012). In the winter, ice cover supports the

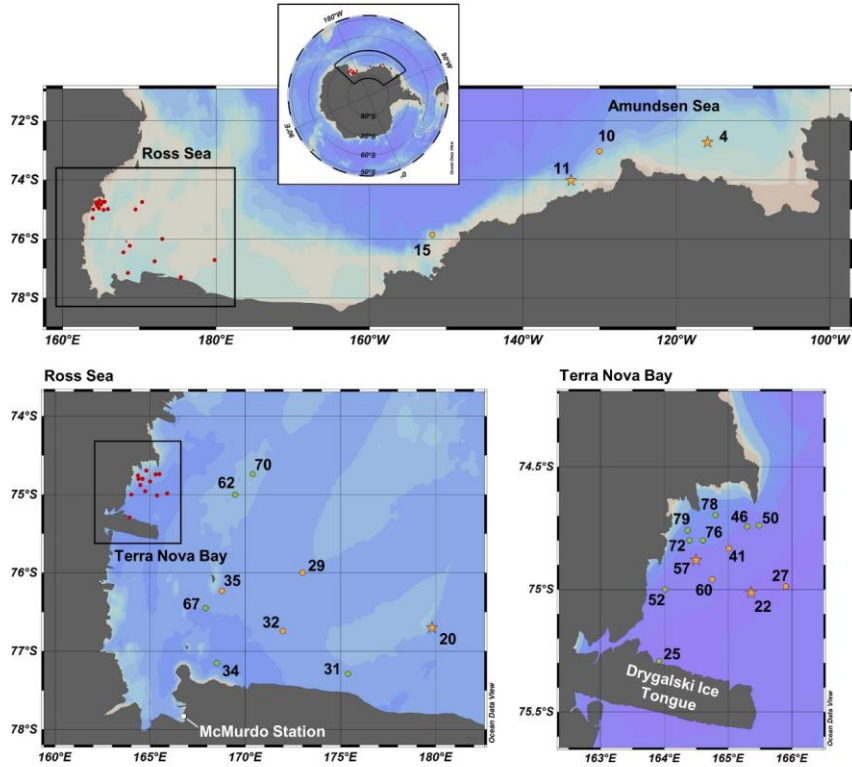
64 turnover of deep waters that allow trace metals like Fe to be redistributed to the upper ocean  
65 (Sedwick and DiTullio, 1997; Sedwick et al., 2011). Phytoplankton blooms in coastal Antarctic  
66 polynyas are dominated by eukaryotes such as diatoms and the haptophyte *Phaeocystis antarctica*  
67 (Arrigo et al., 1999; DiTullio et al., 2003), while cyanobacteria like *Prochlorococcus* and  
68 *Synechococcus*, which are highly abundant in the adjacent South Pacific and South Atlantic gyres,  
69 are near-absent from the phytoplankton community in the Southern Ocean (DiTullio et al., 2003;  
70 Bertrand et al., 2011; Chandler et al., 2016).

71 Cobalt (Co) is an essential trace metal nutrient for many marine plankton and is relatively  
72 scarce in the marine environment, often present in the dissolved phase (dCo) in picomolar  
73 concentrations ( $10^{-12}$  mol L<sup>-1</sup>). Co acts as a cofactor for metalloenzymes like carbonic anhydrase,  
74 a crucial enzyme in the carbon concentrating mechanism of photosynthetic phytoplankton (Sunda  
75 and Huntsman, 1995; Roberts et al., 1997; Kellogg et al., 2020), and vitamin B<sub>12</sub> (cobalamin),  
76 which can be used for the biosynthesis of methionine but is only produced by some bacteria and  
77 archaea (Warren et al., 2002; Bertrand et al., 2013). In the Ross Sea, vitamin B<sub>12</sub> availability has  
78 been observed to co-limit phytoplankton growth with iron (Fe) when bacterial abundance is low  
79 (Bertrand et al., 2007). Some phytoplankton exhibit flexible vitamin B<sub>12</sub> metabolisms and can  
80 express a vitamin B<sub>12</sub>-independent methionine synthase pathway (*metE* gene) instead of the  
81 vitamin B<sub>12</sub>-dependent pathway (*metH* gene), allowing these organisms to thrive in vitamin-  
82 depleted environments (Rodionov et al., 2003; Bertrand et al., 2013; Helliwell, 2017). Recently,  
83 *P. antarctica* was discovered to contain both *metH* and a putative *metE* gene, displaying a  
84 metabolism that is flexible to vitamin B<sub>12</sub> availability (Rao et al., [In review]). Additionally, recent  
85 observations of Zn co-limitation with Fe have been documented in the Ross Sea (Kellogg et al.,  
86 [Submitted]), suggesting a complex landscape of trace metal and vitamin stress interactions in the  
87 otherwise macronutrient-rich waters of coastal Antarctica.

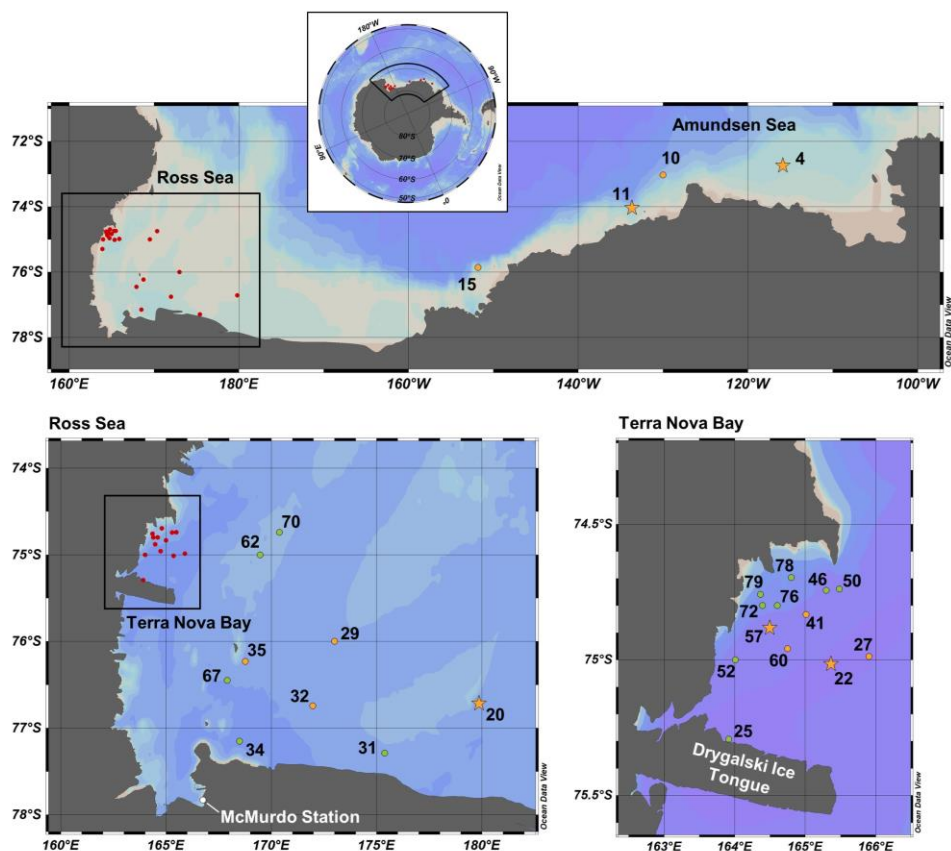
88 Dissolved Co is present as two primary species in the marine environment: a “free” labile  
89 Co(II) species with weakly bound ligands and a Co(III) species that is strongly bound to organic  
90 ligands ( $K_s > 10^{16.8}$ ) (Saito et al., 2005). Labile dCo is considered to be more bioavailable to marine  
91 microbes than strongly-bound dCo, although there is evidence that phytoplankton communities  
92 can access Co in strongly-bound organic ligand complexes (Saito and Moffett 2001) and that  
93 microbial communities may produce extracellular Co ligands that stabilize dCo and prevent its  
94 loss via scavenging to manganese (Mn)-oxide particles (Saito et al., 2005; Bown et al., 2012).  
95 Previous dCo sampling expeditions to the Ross Sea, including two 2005/2006 Controls of Ross  
96 Sea Algal Community Structure (CORSACS) expeditions (Saito et al., 2010) and fieldwork in  
97 2009 that sampled the water column below early spring sea ice in the McMurdo Sound (Noble et  
98 al., 2013), reported relatively high concentrations of labile dCo in the surface Ross Sea when  
99 compared to the tropical and subtropical global oceans, suggesting that labile dCo was fairly  
100 replete and bioavailable to phytoplankton at the time (Saito et al., 2010).

101 This study examines the biogeochemical cycle of Co in the Amundsen and Ross Seas  
102 during the 2017/2018 austral summer as part of the Cobalamin and Iron Co-Limitation of  
103 Phytoplankton Species (CICLOPS) expedition. Here, we present profiles of dCo speciation that  
104 revealed a lower dCo inventory during the 2017/2018 summer bloom compared to that observed  
105 during the 2005/2006 CORSACS expeditions, as well as mostly undetectable concentrations of  
106 labile dCo in the surface ocean. Additional datasets of dissolved zinc (dZn) and cadmium (dCd),  
107 as well as profiles of Co, Zn and Cd uptake rates measured by isotope tracer incubation  
108 experiments suggest that regions of vitamin B<sub>12</sub> and Zn stress within phytoplankton blooms could

109 be driving high demand for bioavailable Co in the surface ocean. The results presented by this  
110 study reveal a substantial perturbation of the Co cycle, and a shift towards vitamin B<sub>12</sub> and/or Zn  
111 limitation, and possible, but unconfirmed, perturbations to the dissolved iron (dFe) cycle in coastal  
112 Antarctic waters impacted by high rates of glacial ice melt and a warming climate.



113



114  
 115 **Figure 1.** Map of CICLOPS stations in coastal Antarctic waters, including insets of stations within  
 116 the Ross Sea and Terra Nova Bay. Dissolved Co, dZn and dCd were analyzed at stations marked  
 117 in yellow, and stations marked in green were analyzed for dZn and dCd, but electrochemical dCo  
 118 measurements were not conducted. At stations marked with a star, Co, Zn and Cd uptake profiles  
 119 are presented in this study. Stations marked in red are shown in more detail in an inset. Note that  
 120 the grey coastline marks both terrestrial coastline and areas of consistent ice, including ice shelves  
 121 and glaciers; this includes the Drygalski Ice Tongue, a glacier to the south of Terra Nova Bay.

122 **2 Methods**

123 2.1 Study area and trace metal sampling

124 Samples were collected along the coastal Antarctic shelf from the Amundsen Sea, Ross  
 125 Sea, and Terra Nova Bay (Fig. 1) during the CICLOPS expedition on the RVIB *Nathanial B.*  
 126 *Palmer* (NBP-1801; December 16, 2017 – March 3, 2018). The expedition track first mapped a

127 [transect from the Amundsen Sea, through the Ross Sea, and ending in Terra Nova Bay \(Stations](#)  
128 [4–22\) over 10 days from December 31, 2017 to January 9, 2018, and then sampled at stations](#)  
129 [between Terra Nova Bay and the western Ross Sea for the remainder of the expedition.](#)

130 Dissolved seawater was collected from full-depth station profiles using a trace metal clean-  
131 sampling rosette deployed on a conducting synthetic line supplied by the U.S. Antarctic Program  
132 (USAP) and equipped with twelve 8 L X-Niskin bottles (Ocean Test Equipment) supplied by the  
133 Saito laboratory ([Woods Hole Oceanographic Institution; Woods Hole, MA, USA](#)). Real-time  
134 trace metal rosette operations allowed for the careful collection of seawater from 10 and 20 m  
135 above the ocean floor to study sediment-water interactions within a potential nepheloid layer. After  
136 deployment, the X-Niskin bottles were transported to a trace metal clean-air van and pressurized  
137 with high-purity (99.999 %) N<sub>2</sub> gas. Seawater samples for [macronutrients](#), dCo and trace metal  
138 analysis were then filtered through acid-washed 0.2 µM Supor polyethersulfone membrane filters  
139 (Pall Corporation, 142 mm diameter) within 3 hours of rosette recovery.

140 To minimize metal contamination of samples, all sample bottles were prepared using trace  
141 metal clean procedures prior to the expedition. The cleaning procedure for dCo sample bottles  
142 entailed soaking sample bottles for ~1 week in Citranox, an acidic detergent, rinsing with Milli-Q  
143 water (Millipore), soaking sample bottles for ~2 weeks in 10% trace metal grade HCl (Optima,  
144 Fisher Scientific), and rinsing with lightly acidic Milli-Q water (< 0.1% HCl). Macronutrient  
145 sample bottles were rinsed with Milli-Q water and soaked overnight in 10% HCl. The procedure  
146 for total dissolved metal sample bottles (dZn and dCd) was identical to that used for dCo bottles  
147 except the Citranox soak step was omitted.

148 Samples for dCo analysis were collected in 60 mL low-density polyethylene (LDPE)  
149 bottles and stored at 4°C until analysis. Duplicate dCo samples were collected: one for at-sea  
150 analysis of labile dCo and total dCo, and another for preservation and total dCo analysis in the  
151 laboratory after the expedition. Preserved total dCo samples were stored with oxygen-absorbing  
152 satchels (Mitsubishi Gas Chemical, model RP-3K), which preserve the sample for long-term  
153 storage and future analysis (Noble et al., 2017; Bundy et al., 2020). Preserved dCo samples were  
154 stored in groups of 6 within an open (unsealed) plastic bag, which was then placed into a gas-  
155 impermeable plastic bag (Ampac) with one oxygen-absorbing satchel per 60 mL dCo sample. The  
156 outer bag was then heat-sealed and stored at 4°C until analysis. [Total dCo concentrations for](#)  
157 [stations 57 and 60 were analyzed in the laboratory, while all other total dCo and labile dCo](#)  
158 [concentrations were analyzed at sea.](#)

159 Samples for total dissolved metal analysis (dZn and dCd) were collected in 250 mL LDPE  
160 bottles and stored double-bagged at room temperature. After ~7 months, the total dissolved metals  
161 samples were acidified to a pH of 1.7 with trace metal grade HCl (Optima, Fisher Scientific), and  
162 were stored acidified for more than one year before instrumental analysis.

## 163 2.2 Dissolved Co and labile dCo analysis

164 Total dCo – the combined fractions of labile and ligand-bound dCo, hereafter simply dCo  
165 – and labile dCo concentrations were analyzed via cathodic stripping voltammetry (CSV) as  
166 described by Saito and Moffett (2001) and modified by Saito et al. (2010) and Hawco et al. (2016).  
167 CSV analysis was conducted using a Metrohm 663 VA and µAutolabIII systems equipped with a  
168 hanging mercury drop working electrode. All reagents were prepared as described in Chmiel et al.  
169 (2022). Most samples were analyzed at sea within 3 weeks of sample collection, and stations 57

Formatted: Indent: First line: 0.5"

170 and 60 were analyzed for labile dCo at sea and their duplicate preserved samples were analyzed  
171 for total dCo in November 2019 in the laboratory.

172 To measure total dCo concentrations, filtered seawater samples were first UV-irradiated in  
173 quartz tubes for one hour in a Metrohm 705 UV Digester to destroy natural ligand-bound Co  
174 complexes. 11 mL of sample was then added to a 15 mL trace metal clean polypropylene vial, and  
175 100  $\mu$ L of 0.1 M dimethylglyoxime (DMG; Sigma Aldrich) ligand and 130  $\mu$ L of 0.5 M N-(2-  
176 hydroxyethyl)piperazine-N-(3-propanesulfonic acid) (EPPS, Sigma Aldrich) buffer was added to  
177 each sample vial. A Metrohm 858 Sample Processor then loaded 8.5 mL of each sample into the  
178 electrode's Teflon cup and added 1.5 mL of 1.5 M NaNO<sub>2</sub> reagent (Merck). The mercury electrode  
179 performed a fast linear sweep from -1.4 V to -0.6 V at a rate of 5 V s<sup>-1</sup> and produced a cobalt  
180 reduction peak at -1.15 V, the voltage at which the Co(DMG)<sub>2</sub> complex is reduced from Co(II) to  
181 Co(0) (Saito and Moffett, 2001). The height of the Co reduction peak is linearly proportional to  
182 the amount of total dCo present in the sample. Peak heights were determined by NOVA 1.10  
183 software. A standard curve was created with 4 additions of 25 pM dCo to each sample, and a type-  
184 I linear regression of the standard addition curve performed by the LINEST function in Microsoft  
185 Excel allowed for the calculation of the initial amount of Co present in the sample.

186 When analyzing labile dCo concentrations, samples were not UV-irradiated so as to only  
187 quantify the free or weakly bound dCo not bound to strong organic ligands. 11 mL of labile  
188 samples were instead allowed to equilibrate with the DMG ligand and EPPS reagent overnight (~8  
189 hours) before analysis to allow time for the labile dCo present in the sample to bind to the DMG  
190 ligand via competitive ligand exchange ( $K > 10^{16.8}$ ). Labile dCo samples were then loaded onto  
191 the Sample Processor and analyzed electrochemically using identical methods as described above  
192 for total dCo samples.

### 193 2.3 Dissolved Co standards and blanks

194 During the CICLOPS expedition, an internal standard consisting of filtered, UV-irradiated  
195 seawater was analyzed for dCo every few days while samples were being analyzed ( $39 \pm 4$  pM,  $n$   
196 = 9). While additional preserved dCo samples were analyzed in the laboratory in November 2019,  
197 triplicate GSC2 GEOTRACES community intercalibration standards were carefully neutralized to  
198 a pH of ~8 using negligible volumes of ammonium hydroxide (NH<sub>4</sub>OH) and analyzed for dCo.  
199 This is the same intercalibration batch originally reported in Table 1 of Chmiel et al. (2022), as  
200 analysis for both expeditions overlapped temporally. The GSC2 standard was determined to have  
201 a dCo concentration of  $80.2 \pm 6.2$  (n = 3), a value that is very similar to the one reported by Hawco  
202 et al., (2016) ( $77.7 \pm 2.4$ ). Currently, no official community consensus for dCo in the GSC2  
203 intercalibration standard exists.

204 Analytical blank measurements for each reagent batch (a unique combination of DMG,  
205 EPPS, and NaNO<sub>2</sub> reagent batches) were measured to determine any Co contamination due to  
206 reagent impurities. Blanks were prepared in triplicate with UV-irradiated surface seawater passed  
207 through a column with Chelex 100 resin beads (Bio-Rad) to remove metal contaminants, then UV-  
208 irradiated again. Chelex beads were prepared as described in Price et al. (2013) to remove organic  
209 impurities from leaching into the eluent. For the 5 batches of reagents used on this expedition, the  
210 analytical blanks were found to be 2.3 pM, 4.0 pM, 10.1 pM, 15.6 pM, and 8.6 pM dCo, with an  
211 average of 8.1 pM Co. The analytical blank detected for the laboratory-run total dCo samples was  
212 1.0 pM. It should be noted that blank values above 10 pM are considered high for this method.  
213 Analytical blank values were subtracted from the measured Co values determined with the

214 respective reagent batch. The average standard deviation within each triplicate batch of blanks (1.3  
 215 pM) was used to estimate the analytical limit of detection ( $3 \times$  blank standard deviation) of 4 pM.  
 216 When detectable dCo concentrations were found below the 4 pM detection limit, their values were  
 217 preserved in the dataset and flagged as below the detection limit (<DL). In cases where no dCo or  
 218 labile dCo were detected (i.e., when no peak was measurable and/or the dCo value predicted was  
 219 < 0 pM), values of 0 pM were assigned for the purposes of plotting and selecting statistical analysis  
 220 and were flagged as not detected (n.d.) as well as <DL in the dataset; although these concentrations  
 221 were not detectable with our methodology, we believe the incredibly low concentrations of dCo  
 222 and labile dCo observed on this expedition were meaningful, and that removing these values from  
 223 our analysis misrepresents the data and would skew the results to appear higher than was observed.

224 **Table 1.** Mean dCo and labile dCo values measured in the surface ocean (10 m) and the deep  
 225 ocean (> 100 m) in the three regions sampled. One dCo sample and numerous labile dCo samples  
 226 were determined to be below the analytical detection limit (<DL) of 4 pM. Only using the values  
 227 measured above the detection limit would artificially inflate the calculation of the mean value;  
 228 instead, samples measured between 0 and the DL were left unaltered as their originally measured  
 229 value and samples with no detected concentrations of dCo or labile dCo (n.d.) were adjusted to 0  
 230 pM. The number of samples included in the mean calculation that are <DL is indicated by  $n_{<DL}$ .

231

Surface (10 m)					
Region	n	dCo <sub>mean</sub> [pM]	n <sub>&lt;DL</sub> for dCo	Labile dCo <sub>mean</sub> [pM]	n <sub>&lt;DL</sub> for labile dCo
Amundsen Sea	4	28 ± 7	0	5 ± 6	2
Ross Sea	4	28 ± 12	0	1 ± 2 <sup>a</sup>	4
Terra Nova Bay	5	11 ± 7	1	n.d. <sup>b</sup>	5

Deep (> 100 m)					
Region	n	dCo <sub>mean</sub> [pM]	n <sub>&lt;DL</sub> dCo	Labile dCo <sub>mean</sub> [pM]	n <sub>&lt;DL</sub> Labile dCo
Amundsen Sea	30	41 ± 5	0	4 ± 4	14
Ross Sea	32	46 ± 8	0	9 ± 7	9
Terra Nova Bay	34	39 ± 18	0	6 ± 8	18

232

Surface (10 m)					
Region	n	dCo <sub>mean</sub> [pM]	n <sub>&lt;DL</sub> dCo	Labile dCo <sub>mean</sub> [pM]	n <sub>&lt;DL</sub> Labile dCo
Amundsen Sea	4	28 ± 7	0	5 ± 6	2
Ross Sea	4	28 ± 12	0	1 ± 2 <sup>a</sup>	4
Terra Nova Bay	5	11 ± 7	1	UD <sup>b</sup>	5

Deep (> 100 m)					
Region	n	dCo <sub>mean</sub> [pM]	n <sub>&lt;DL</sub> dCo	Labile dCo <sub>mean</sub> [pM]	n <sub>&lt;DL</sub> Labile dCo
Amundsen Sea	30	41 ± 5	0	4 ± 4	14
Ross Sea	32	46 ± 8	0	9 ± 7	9
Terra Nova Bay	34	39 ± 18	0	6 ± 8	18

233

234 <sup>a</sup> Of the 4 surface samples analyzed for labile dCo in the Ross Sea, 3 were n.d. and the fourth  
 235 contained 3.5 pM labile dCo.



236 <sup>b</sup> All surface samples in Terra Nova Bay were n.d. for labile dCo.

#### 237 2.4 Dissolved Zn and Cd analyzed by ICP-MS

238 Total dissolved trace metal samples were analyzed for dZn and dCd using isotope dilution  
239 and inductively coupled plasma mass spectrometry (ICP-MS) as described in Kellogg et al.  
240 (Submitted) based on methodology described in Cohen et al. (2021). Briefly, 15 mL of acidified  
241 filtered seawater samples were spiked with an acidified mixture of stable isotopes including <sup>67</sup>Zn,  
242 and <sup>110</sup>Cd, among other metal stable isotopes, and pre-concentrated via a solid phase extraction  
243 system seaFAST-pico (Elemental Scientific) to an elution volume of 500 µL. The samples were  
244 then analyzed using an iCAP-Q ICP-MS (Thermo Scientific) and concentrations were determined  
245 using a multi-elemental standard curve (SPEX CertiPrep).

#### 246 2.5 Co, Zn and Cd uptake rates via isotope incubations

247 Co, Zn and Cd uptake rates were quantified using incubations of collected marine microbial  
248 communities spiked with stable or radioisotopes to trace the conversion of dissolved trace metal  
249 into the particulate phase. Briefly, unfiltered seawater used for the incubation uptake experiments  
250 was collected from the trace metal rosette, and the Co, Zn and Cd uptake incubations were spiked  
251 with 0.1 pM <sup>57</sup>CoCl<sub>2</sub>, 2 nM <sup>67</sup>ZnO and 300 pM <sup>110</sup>CdO, respectively. All incubation bottles were  
252 then sealed and placed in a flow-through shipboard incubator on the deck that exposed the  
253 incubations to a natural day/night cycle and surface-temperature seawater for 24 hours. The  
254 incubator was shielded by black mesh screening to allow 20% ambient light penetration.  
255 Incubation biomass was collected by vacuum filtration onto acid-rinsed 3 µm Versapor filters  
256 (Pall). The <sup>57</sup>Co incubation filters were stored at room temperature in Petri dishes prior to  
257 radiochemical gamma-ray counting both at sea and in the laboratory, and the <sup>67</sup>Zn and <sup>110</sup>Cd  
258 incubation filters were stored at -80 °C in acid-rinsed cryovials until ICP-MS analysis in the  
259 laboratory. See Kellogg et al. (Submitted), Rao 2020 and Kellogg (2022) for full methodology and  
260 instrumental analysis.

#### 261 2.6 Pigment and phosphate analysis

262 Phytoplankton pigment samples were collected from a non-trace metal rosette deployed  
263 separately from the trace metal rosette, and were filtered via filtration and analyzed for select  
264 pigments by high-performance liquid chromatography (HPLC) as described in DiTullio and  
265 Geesey (2003). Macronutrient samples were collected from the trace metal rosette alongside dCo  
266 samples and were filtered using the same methodology as dCo and total metal samples (see above).  
267 Samples were collected in 60 mL high-density polyethylene (HDPE) bottles and were stored  
268 frozen until analysis. Dissolved PO<sub>4</sub> concentrations were determined by Joe Jennings at Oregon  
269 State University via the molybdenum blue method (Bernhardt and Wilhelms, 1967) using a  
270 Technicon AutoAnalyzer II attached to an Alpkem autosampler.

#### 271 2.7 Historical dCo and pigment data

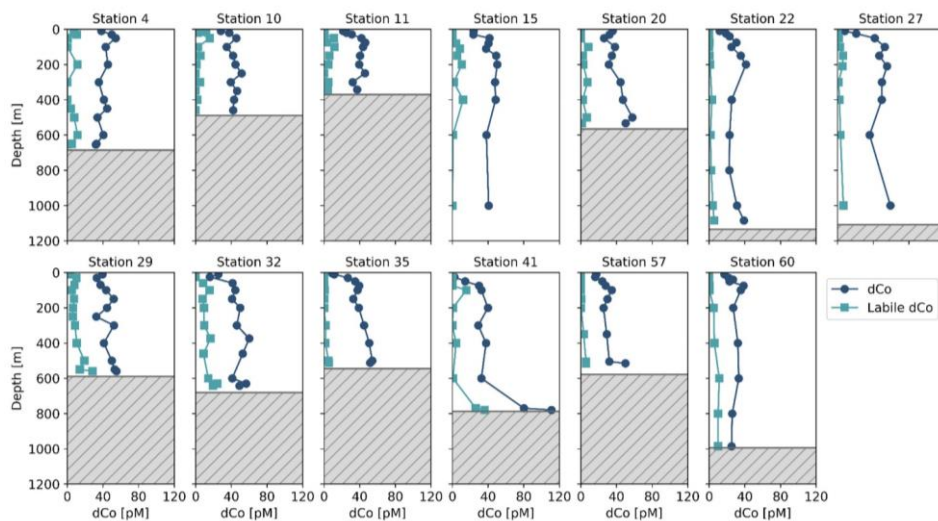
272 In this study, dCo profiles from the CICLOPS expedition are compared to those from  
273 previous fieldwork in the Ross Sea, including the Controls of Ross Sea Algal Community Structure  
274 (CORSACS) expeditions: CORSACS-1 (NBP-0601; December 27, 2005 – January 23, 2006) and  
275 CORSACS-2 (NBP-0608; November 8, 2006 – December 3, 2006), reported in Saito et al. (2010),  
276 and fieldwork sampling the water column under the sea ice of the McMurdo Sound (November 9

277 – 23, 2009), reported in Noble et al. (2013). [The locations of stations used in this study from the](#)  
 278 [CORSACS-1 expedition, CORSACS-2 expedition, and McMurdo Sound fieldwork are given with](#)  
 279 [respect to CICLOPS stations in Fig. A1.](#) Dissolved cobalt and pigment data from these three  
 280 fieldwork expeditions were sampled and analyzed with comparable methodologies as those used  
 281 on the CICLOPS expedition, and the CORSACS data are accessible online at [https://www.bco-](https://www.bco-dmo.org/dataset/3367)  
 282 [dmo.org/dataset/3367](https://www.bco-dmo.org/dataset/3367).

## 283 2.8 Statistical Analysis

284 The linear regressions presented in this study are two-way (type-II) linear regressions, with  
 285 the exception of the standard addition curves used to calculate dCo concentrations (Sect. 2.2).  
 286 Two-way regressions are ideal for stoichiometric ratios because they allow for error in both the x  
 287 and y parameters and do not assume dependence between the x and y axes. The two-way regression  
 288 function used in this study was rewritten to Python from a MATLAB file (lsqfitma.m) originally  
 289 written by Ed Pelzer circa 1995 (Chmiel et al., 2022) and is available at [https://github.com/rebecca-](https://github.com/rebecca-chmiel/GP15)  
 290 [chmiel/GP15](https://github.com/rebecca-chmiel/GP15).

291 Independent t-tests were performed using the stats.ttest\_ind function within statistical  
 292 function module of the SciPy Python library.



293 **Figure 2.** Dissolved Co and labile dCo full-depth profiles from the CICLOPS expedition to the  
 294 Amundsen Sea (Stations 4, 10, 11, 15), Ross Sea (Stations 20, 29, 32, 35) and Terra Nova Bay  
 295 (Stations 22, 27, 41, 57, 60). The top of the grey box marks the location of the seafloor.

## 297 3 Results

### 298 3.1 Dissolved Co distribution and speciation

299 During the CICLOPS expedition, full-depth profiles of dCo and labile dCo samples were  
 300 analyzed from 13 stations in the Amundsen Sea (Stations 4, 10, 11, 15), the Ross Sea (Stations 20,

301 29, 32, 35) and Terra Nova Bay (Stations 22, 27, 41, 57, 60; Fig. 1). The resulting dCo profiles  
302 (Fig. 2) show depletion in the surface ocean consistent with a nutrient-type profile; at 10 m depth,  
303 dCo concentrations were found to be  $28 \pm 7$  pM in the Amundsen Sea ( $n = 4$ ),  $28 \pm 12$  pM in the  
304 Ross Sea ( $n = 4$ ), and only  $11 \pm 7$  pM in Terra Nova Bay ( $n = 5$ ; Table 1). Labile dCo distributions  
305 generally followed those of dCo, and also showed strong depletion in the surface ocean. In the  
306 Amundsen and Ross Seas, surface ( $\sim 10$  m) labile dCo concentrations ranged between 12 pM at  
307 station 10 and undetected (n.d.) concentrations at stations 15, 20, 32 and 35. In Terra Nova Bay,  
308 no surface labile dCo concentrations were detected at any of the 5 stations sampled, indicating that  
309 the dCo inventory was dominated by the strongly ligand-bound dCo fraction.

310 In the deep ocean ( $\geq 100$  m depth), dCo distributions were relatively consistent throughout  
311 the water column, with the exception of elevated concentrations of dCo at near-bottom depths. The  
312 Amundsen Sea, Ross Sea, and Terra Nova Bay all displayed similar deep ( ~~$\geq 100$  m depth~~) dCo  
313 concentrations of  $41 \pm 5$  pM ( $n = 30$ ),  $46 \pm 8$  pM ( $n = 32$ ), and  $39 \pm 18$  pM ( $n = 34$ ), respectively  
314 (Table 1). The high standard deviation of deep dCo in Terra Nova Bay is partially driven by the  
315 elevated near-seafloor signal at Station 41 (~~770 m and 780 m~~); when the two deepest points at  
316 Station 41 are omitted (~~770 m and 780 m~~), the average deep dCo in Terra Nova Bay was  $36 \pm 10$   
317 pM. The CICALOPS expedition included regular near-bottom sampling as allowed by the altimeter  
318 aboard the trace metal rosette. As a result, many of the deepest profile samples contained elevated  
319 concentrations of dCo and labile dCo along the seafloor, including stations 20, 22, 27, 29, 32, 41  
320 and 57. This deep dCo signal was particularly observable in stations where two near-seafloor  
321 samples were taken: one  $\sim 10$  m above the seafloor and a second  $\sim 20$  m above the seafloor. At  
322 stations 41 and 57, the elevated near-seafloor dCo signal was pronounced (Fig. 2); the samples  
323  $\sim 10$  m above the seafloor contained 111 pM and 50 pM dCo, respectively, which represents a 31  
324 pM and 18 pM increase, respectively, from the samples collected  $\sim 20$  m above the seafloor. This  
325 finding indicates that dCo was elevated in a narrow band close to the seafloor, and it is likely that  
326 dCo concentrations continued to increase in the 10 m between the deepest samples and the seafloor.

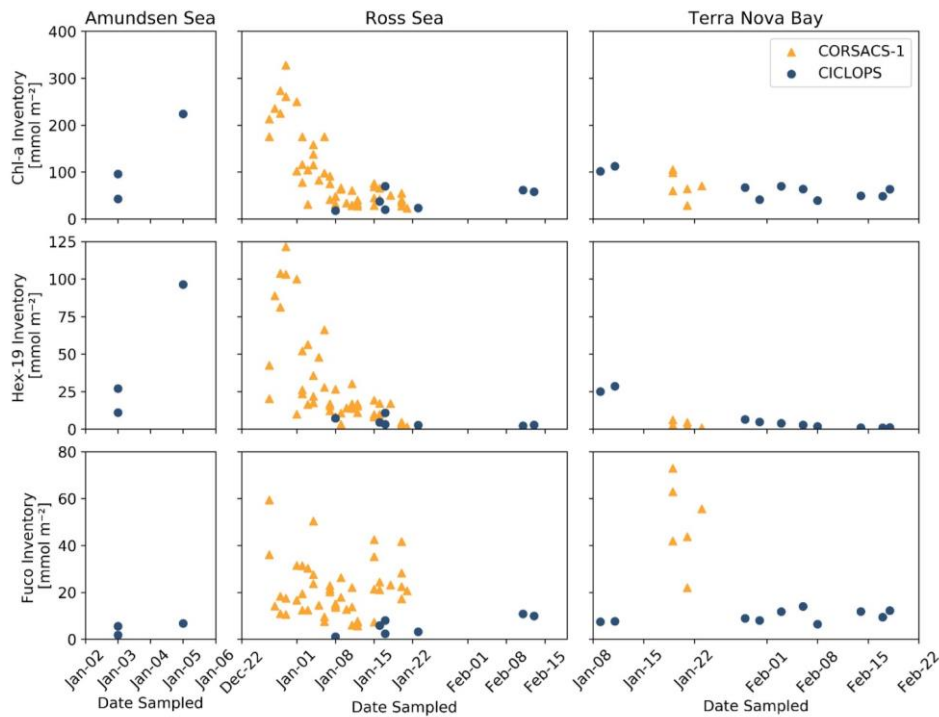
### 327 3.2 Phytoplankton communities in the Amundsen Sea, Ross Sea and Terra Nova Bay

328 Stations 11, 15, 22 and 27 exhibited high surface chlorophyll-a (Chl-a) fluorescence ( $17$ –  
329  $42$  mg  $m^{-3}$  at 10 m), characteristic of phytoplankton blooms. The Amundsen Sea stations displayed  
330 high concentrations of 19'-hexanolyoxyfucoxanthin (19'-Hex), a pigment commonly used as a  
331 proxy for haptophyte biomass. In the coastal Southern Ocean, 19'-Hex is often correlated with  
332 *Phaeocystis antarctica* (DiTullio and Smith, 1996; DiTullio et al., 2003), and it is typical to find  
333 concentrated blooms of *P. antarctica* in these regions, particularly during the highly productive  
334 spring blooms of the Antarctic polynyas (Arrigo et al., 1999; DiTullio et al., 2000). The pigment  
335 fucoxanthin (Fuco) is commonly used as a proxy for diatom biomass, although it can also be  
336 produced by haptophytes like *P. antarctica* growing under Fe-replete conditions (DiTullio et al.,  
337 2003; DiTullio et al., 2007); Fuco was observed at stations throughout the expedition and tended  
338 to be relatively consistent throughout the CICALOPS stations, particularly in comparison to 19'-  
339 Hex, which displayed very high concentrations at some stations and much lower concentrations at  
340 others. In general, higher concentrations of Fuco were observed within Terra Nova Bay as well as  
341 at stations sampled later in the summer season. This is consistent with past observations of summer  
342 diatom blooms, which tend to occur after the annual spring bloom where and when dFe is available  
343 (Sedwick et al., 2000; Pelloquin and Smith, 2007; Saito et al., 2010).

344 The upper ocean inventories of three pigments, 19'-Hex, Fuco and Chl-a, a proxy for  
 345 general phytoplankton biomass in the Southern Ocean, were estimated via trapezoidal integration  
 346 of their profiles between 5 and 50 m depth and compared to the 2005/2006 summer bloom  
 347 observed on the CORSACS-1 expedition (Fig. 3). In the Ross Sea and Terra Nova Bay, CICLOPS  
 348 stations contained smaller inventories of Chl-a and 19'-Hex compared to the Amundsen Sea, likely  
 349 reflecting the end of the spring bloom and transition to a summer phytoplankton assemblage in  
 350 these regions. One noticeable difference between the overlapping 2006 and 2018 January seasons  
 351 is the larger Fuco inventory in 2006 in both the Ross Sea and Terra Nova Bay compared to the  
 352 2018 season, indicating a larger presence of diatom biomass during the CORSACS-1 expedition  
 353 compared to the CICLOPS expedition despite relatively similar Chl-a inventories.

354 3.3 dZn, dCd and trace metal uptake rates

355 Dissolved Cd and Zn profiles, as well as trace metal uptake rate ( $\rho M$ ) profiles for Co, Zn  
 356 and Cd from the CICLOPS expedition were originally presented in Rao (2020) and Kellogg  
 357 (2022). This study presents a comparison between dCo distribution and the distribution and uptake  
 358 of dZn and dCd, two trace metals linked with Co biogeochemical cycling since all three metals are  
 359 known to share similar uptake transporter pathways and can be interchangeably utilized as  
 360 cofactors within specific classes of the enzyme carbonic anhydrase (Sunda and Huntsman, 1995,  
 361 2000; Saito and Goepfert, 2008; Kellogg et al., 2020, 2022).



362

363 **Figure 3.** Upper ocean inventories of Chlorophyll-a (Chl-a), 19'-hexanolyoxyfucoxanthin (19'-  
 364 Hex) and fucoxanthin (Fuco) plotted over the austral summer season for both the 2005/2006  
 365 CORSAKS-1 and 2017/2018 CICLOPS expeditions. Inventories were estimated via trapezoidal  
 366 integration of the pigment depth profiles between 5 and 50 m depth. Note that the dates along the  
 367 x-axis are not continuous between plots of each region, and the y-axis scales differ among the 3  
 368 pigments.

369 The dZn and dCd profiles observed on the CICLOPS expedition displayed nutrient-like  
 370 structure, with depleted concentrations near the surface (Fig. 4). In the deep ocean ( $\geq 100$  m), dZn  
 371 and dCd concentrations were relatively uniform, displaying average deep concentrations of  $4.6 \pm$   
 372  $1.1$  ~~ppM~~  $\mu\text{M}$  ( $n = 182$ ) and  $700 \pm 90$   $\mu\text{M}$ , respectively (Table 2). Average dissolved metal  
 373 concentrations in the surface ocean (10 m depth) were higher in the Amundsen Sea ( $2.5 \pm 1.2$  nM  
 374 dZn;  $450 \pm 170$  pM Cd) compared to the Ross Sea ( $1.1 \pm 1.2$  nM dZn;  $250 \pm 170$  pM dCd) and  
 375 Terra Nova Bay ( $0.87 \pm 0.42$  nM dZn;  $130 \pm 170$  pM dCd). This trend of decreasing surface  
 376 dissolved metals from the Amundsen to Terra Nova Bay was mirrored in the dCo distributions,  
 377 and could be explained by the seasonal drawdown of metal nutrients in the mixed layer over time,  
 378 differences in the metal uptake of phytoplankton in the different regions, or both phenomenon  
 379 occurring simultaneously.

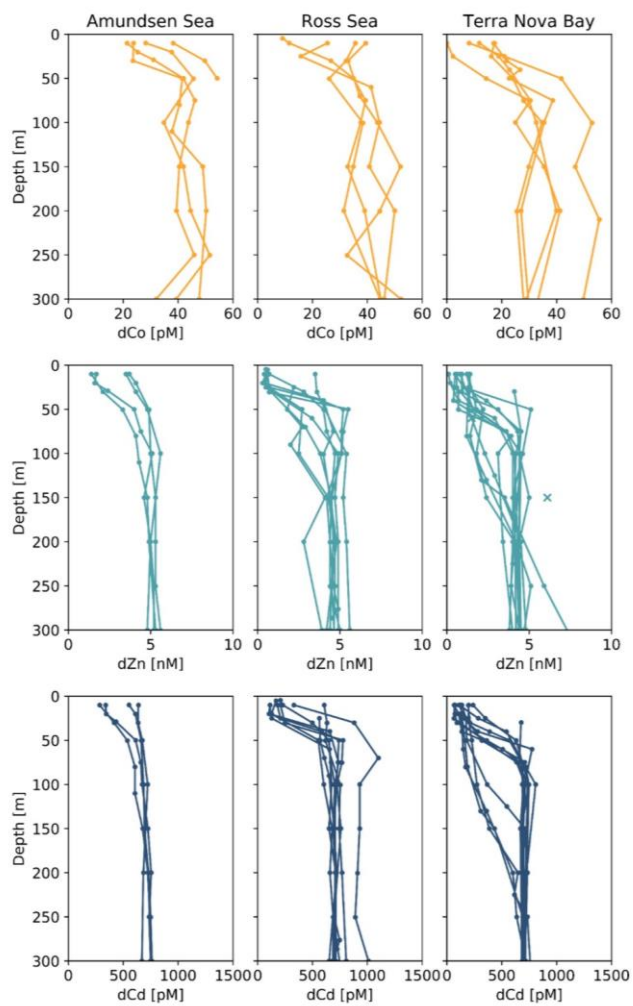
380 At Stations 4, 11, 20, 22 and 57, uptake rates of Co, Zn and Cd within ~~surface~~-seawater  
 381 collected from 0–200 m were determined via spiked-isotope incubations (Rao, 2020; Kellogg,  
 382 2022). The relative ratios of the resulting uptake profiles from biomass collected onto  $3 \mu\text{m}$  filters  
 383 provide insight into the demand for Co, Zn and Cd of eukaryotic phytoplankton in coastal  
 384 Antarctica (Fig. 5). Note that Co uptake within the bacterial size fraction ( $0.2\text{--}3 \mu\text{m}$ ) was also  
 385 analyzed and the results are presented in Rao (2020), but here we present the results of the  
 386 eukaryotic size fraction ( $> 3 \mu\text{m}$ ) to best represent the eukaryotic phytoplankton community  
 387 present and compare to the Zn and Cd uptake experiments. It should be noted that uptake rates  
 388 measured via tracer addition and shipboard incubations represent potential uptake and may be  
 389 overestimations of the environmental nutrient uptake rates because the isotope tracer addition was  
 390 labile – not at equilibrium with the natural seawater ligands – and could have perturbed the  
 391 natural micronutrient inventories. The  $^{57}\text{CoCl}_2$  addition ( $0.1 \mu\text{M}$ ) was likely a small enough  
 392 addition that the inventory was not significantly disturbed, but added concentrations of  $^{67}\text{ZnO}$  ( $2$   
 393  $\text{nM}$ ) and  $^{110}\text{CdO}$  ( $300 \mu\text{M}$ ) ~~spikes~~ were not tracer-level additions and necessarily increased the  
 394 existing trace metal inventories, possibly leading to the overestimation of total metal uptake rates  
 395 (Rao, 2020; Kellogg, 2022).

396 **Table 2.** Mean dZn and dCd values from the surface ocean (10 m) and the deep ocean ( $> 100$  m)  
 397 in the three regions sampled.

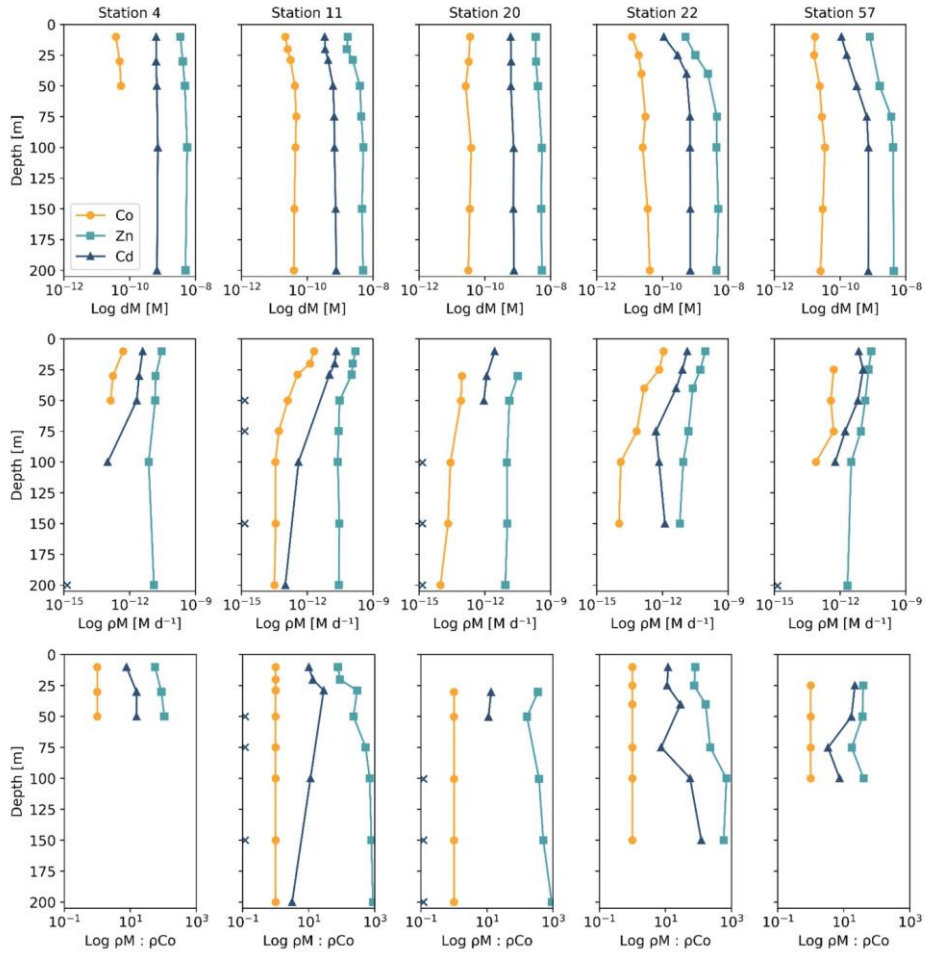
Surface (10 m)				
Region	dZn <sub>mean</sub> [nM]	n <sub>dZn</sub>	dCd <sub>mean</sub> [pM]	n <sub>dCd</sub>
Amundsen Sea	2.6 ± 1.2	4	450 ± 170	4
Ross Sea	1.1 ± 1.2	6	250 ± 170	7
Terra Nova Bay	0.87 ± 0.42	11	130 ± 60	11
All	1.3 ± 1.0	21	230 ± 170	22
Deep (> 100 m)				
Region	dZn <sub>mean</sub> [nM]	n <sub>dZn</sub>	dCd <sub>mean</sub> [pM]	n <sub>dCd</sub>
Amundsen Sea	5.4 ± 0.6	30	730 ± 40	30
Ross Sea	4.7 ± 0.6	65	740 ± 80	65
Terra Nova Bay	4.3 ± 1.4	87	670 ± 100	90
All	4.6 ± 1.1	182	700 ± 90	185

398

399 Of the five stations with uptake rate data from all three trace metals of interest, four  
400 (Stations 4, 11, 20 and 22) were from a transect conducted from the Amundsen Sea to Terra Nova  
401 Bay, and were sampled within a span of 10 days from December 31, 2017 to January 9, 2018,  
402 while the last station (Station 57) was sampled later in the summer on February 6, 2018; this range  
403 of stations allows us to assess the uptake stoichiometry along both spatial (location) and time  
404 (bloom progression) dimensions. The  $\rho M$  profiles displayed an increase in metal uptake of Co, Zn  
405 and Cd towards the surface, a shape which was mirrored in the lower dissolved trace metal  
406 concentrations of the surface ocean, suggesting the influence of phytoplankton uptake on the  
407 drawdown of micronutrients in the photic zone. The stoichiometry of  $\rho M$  among Co, Zn and Cd  
408 tended to directly follow the metals' availability as dissolved species: Co, which is present at the  
409 lowest concentrations of  $\sim 10^{-11}$  M, was taken up at rates ranging between  $10^{-13}$  and  $10^{-12}$  M d<sup>-1</sup>;  
410 Cd, at concentrations of  $\sim 10^{-10}$  M, was taken up at rates of  $10^{-12}$  to  $10^{-11}$  M d<sup>-1</sup>; and Zn, present in  
411 the highest concentration of  $\sim 10^{-9}$  M, was taken up at rates of  $10^{-12}$  to  $10^{-10}$  M d<sup>-1</sup>. This observation  
412 reveals order-of-magnitude differences in biological uptake between the three metals, matching  
413 patterns of metal availability in the water column.

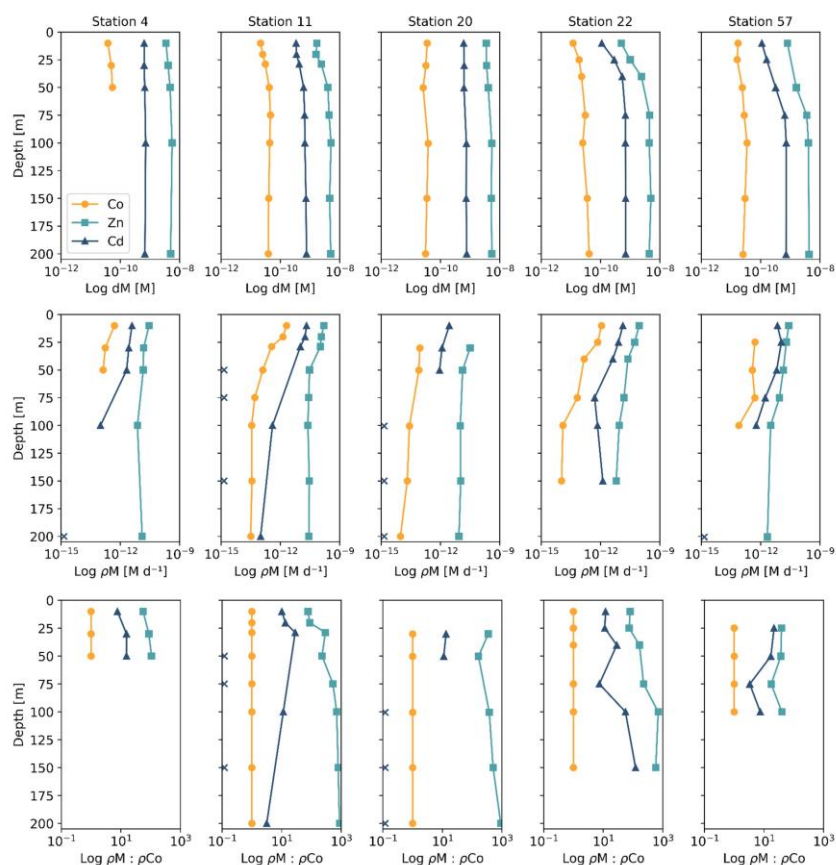


414  
415 **Figure 4.** Upper ocean trace metal depth profiles of dCo, dZn and dCd, by region (left panels,  
416 Amundsen Sea; middle panels, Ross Sea; right panels, Terra Nova Bay). Outliers are marked with  
417 an 'x'. Dissolved Zn and Cd profile data are further described in Kellogg (2022).



418





419 **Figure 5.** Depth profiles of dissolved metals (dM; top), trace metal uptake rates ( $\rho M$ ; middle), and  
 420 trace metal uptake rates normalized to the uptake rate of dCo ( $\rho M : \rho Co$ ), plotted along a log scale.  
 421 Stations 4 and 11 are from the Amundsen Sea, Station 20 is from the Ross Sea, and Stations 22  
 422 and 57 are from Terra Nova Bay. Depths at which an uptake rate is below detection (specifically  
 423 for  $\rho Cd$ ) are marked with an 'x' along the y-axis. Co trace metal uptake data are further described  
 424 in Rao (2020) and Zn and Cd uptake data are further described in Kellogg (2022).  
 425

#### 426 4 Discussion

##### 427 4.1 Biogeochemical Co cycle processes observed via dCo profiles and dCo : dPO<sub>4</sub><sup>3-</sup> stoichiometry

428 Low surface ocean dCo and labile dCo concentrations are attributable to uptake by  
 429 phytoplankton and bacteria in the Southern Ocean, giving the dCo and labile dCo *vertical* profiles  
 430 a distinct nutrient-like shape (Fig. 2). The labile dCo fraction was extremely low or below the limit  
 431 of detection in surface waters, particularly within Terra Nova Bay, indicating strong drawdown of  
 432 the labile fraction and near 100% complexation of dCo in the water column. Labile dCo is

Formatted: Font: Italic

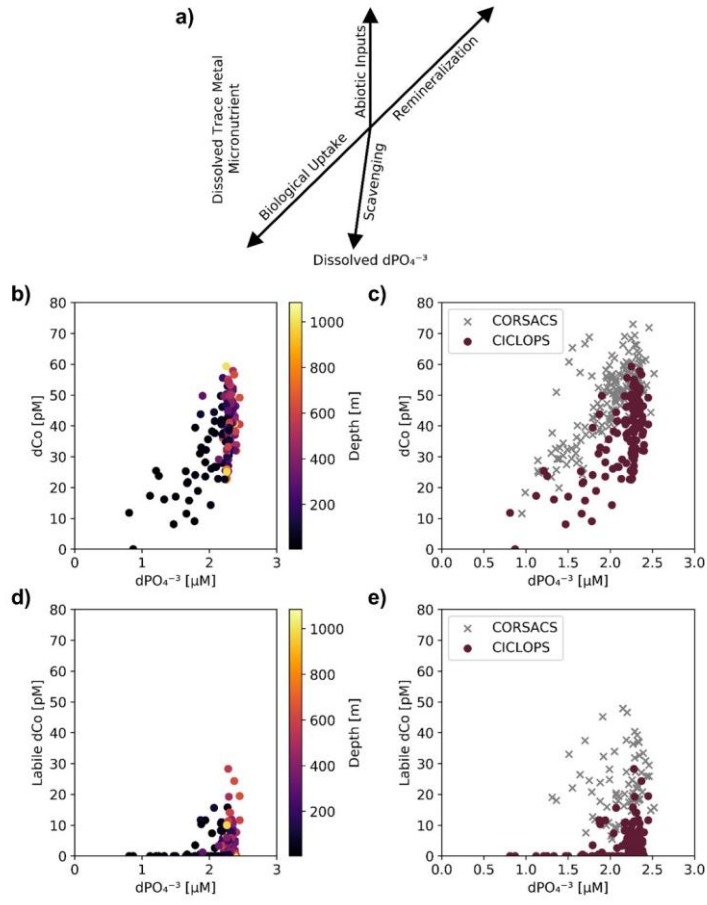
Formatted: Font: Italic

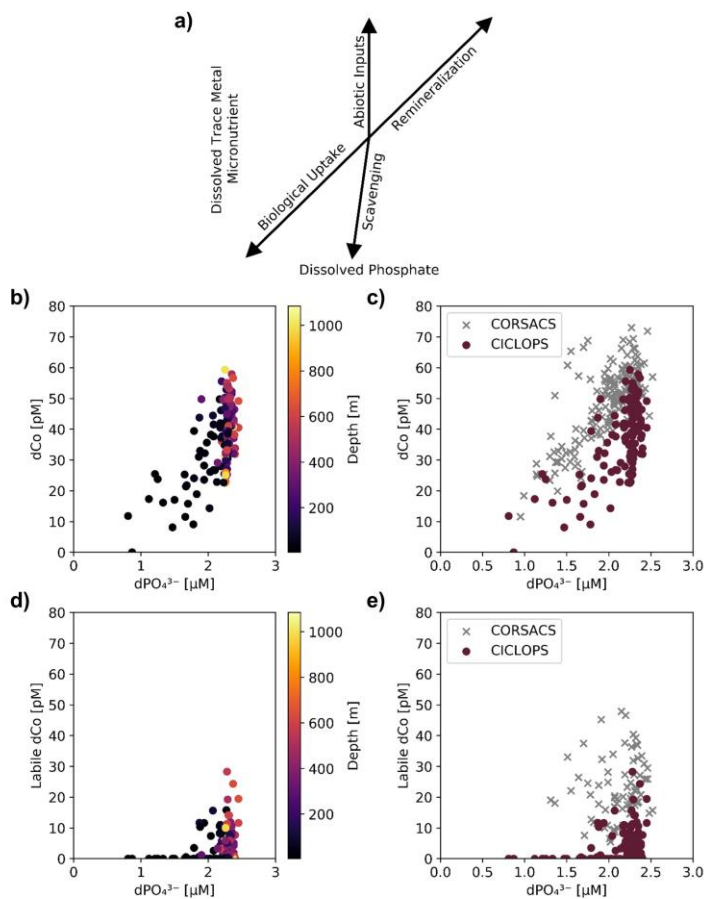
Formatted: Font: Italic

433 considered to be more bioavailable than strongly-bound dCo and thus is likely preferentially taken  
434 up by microbes when available. This labile dCo may then be rapidly cycled by phytoplankton in  
435 the mixed layer and any labile dCo released via remineralization, cell lysis, or grazing would be  
436 promptly taken up by other algae and microbes. A rapid turnover of labile dCo suggests a high  
437 demand for bioavailable Co from the surface phytoplankton community.

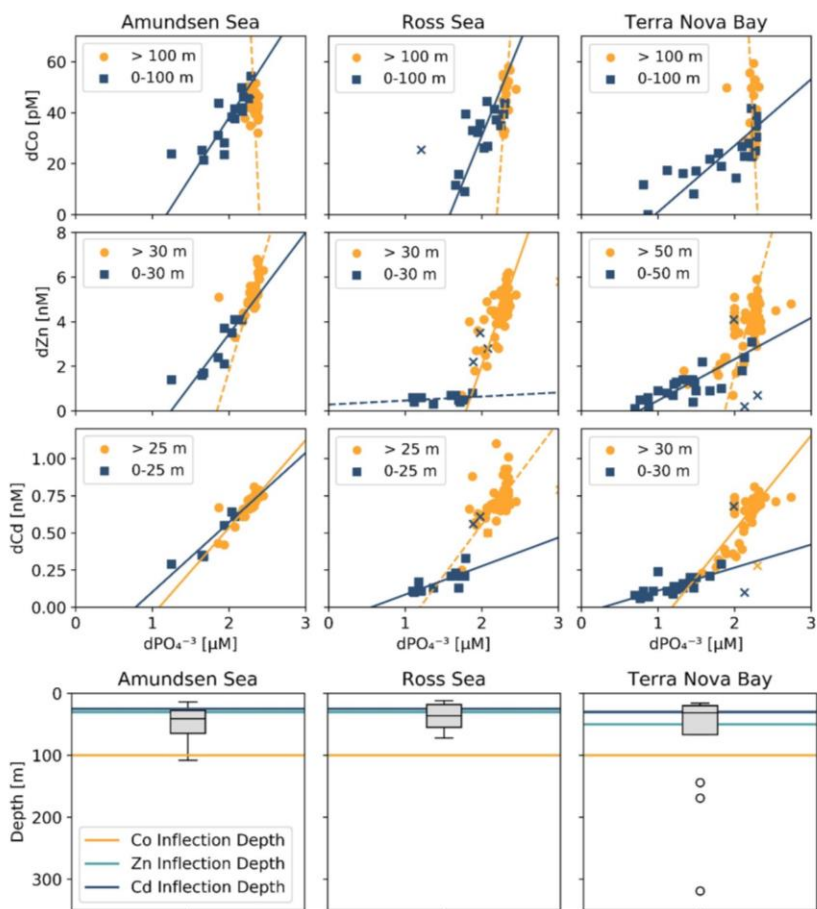
438 Dissolved Co and PO<sub>4</sub> displayed a generally positive relationship in the upper ocean, which  
439 is indicative of the co-cycling of both nutrients via phytoplankton uptake and remineralization  
440 (Fig. 6a). The processes of biological uptake and remineralization, when observed along dCo vs.  
441 dPO<sub>4</sub><sup>3-</sup> axes, can be represented by vectors with positive slopes and opposite directionality. Abiotic  
442 dCo inputs and Co scavenging processes can be represented by vertical or near-vertical vectors  
443 because they decouple the cycling of dCo and dPO<sub>4</sub><sup>3-</sup>. The positive dCo vs. dPO<sub>4</sub><sup>3-</sup> linear  
444 relationship that is often observed within the ocean's mixed layer can exhibit a variety of slopes  
445 that are dictated by the nutrient uptake and remineralization stoichiometry of the microbial  
446 community (Saito et al., 2017). On CICLOPS, the dCo vs. dPO<sub>4</sub><sup>3-</sup> relationship displayed a  
447 drawdown of both dCo and dPO<sub>4</sub><sup>3-</sup> in the upper ocean, and the labile dCo vs. dPO<sub>4</sub><sup>3-</sup> relationship  
448 revealed the stark lack of labile dCo throughout the upper ocean (Fig. 6b,d). The dCo vs. dPO<sub>4</sub><sup>3-</sup>  
449 slope in the upper ocean (0–100 m depth) was found to be distinct for each of the three regions  
450 sampled on the expedition; the Ross Sea displayed the highest slope ( $74 \pm 18 \mu\text{mol} : \text{mol}$ ), followed  
451 by the Amundsen Sea ( $47 \pm 9 \mu\text{mol} : \text{mol}$ ) and Terra Nova Bay, which displayed the lowest dCo  
452 vs. dPO<sub>4</sub><sup>3-</sup> slope ( $26 \pm 4 \mu\text{mol} : \text{mol}$ ; Fig. 7; Table 3). These slopes reflect a relatively wide range  
453 of dCo stoichiometries that vary by a factor of 2.8 between the lowest and highest slopes observed.  
454 For comparison, the 2005/2006 CORSACS-1 and CORSACS-2 Ross Sea data points were pooled  
455 and the dCo vs. dPO<sub>4</sub> slope was recalculated (originally reported as  $37.6 \mu\text{mol} : \text{mol}$  between 5–  
456 500 m depth; Saito et al., 2010) to fall within the same depth window (0–100 m). The resulting  
457 slope fell within the range of slopes observed on CICLOPS ( $49 \pm 4 \mu\text{mol} : \text{mol}$ ;  $R^2 = 0.57$ ;  $n =$   
458 106).

459 The range of dCo vs. dPO<sub>4</sub><sup>3-</sup> slopes reflects the elasticity of cobalt uptake stoichiometry in  
460 the upper ocean, which varies by microbial community and the availability of dCo and other  
461 nutrients. Due to the number of factors that can affect the environmental stoichiometry of trace  
462 metal nutrients, the dCo vs. dPO<sub>4</sub><sup>3-</sup> slope must be interpreted alongside other information about  
463 the marine environment, such as the available dCo inventory and the local nutrient limitation  
464 regime, making global comparisons of dCo : dPO<sub>4</sub><sup>3-</sup> stoichiometry complex. The lower  
465 stoichiometric slope observed in Terra Nova Bay compared to the Ross and Amundsen Seas likely  
466 indicates not a lack of demand for Co by phytoplankton, but the low availability of Co in the  
467 surface ocean despite high demand for the metal. Terra Nova Bay was found to have the lowest  
468 average surface dCo, dZn and dCd concentrations of the three regions studied, and both Terra  
469 Nova Bay stations where  $\rho\text{Co}$  was measured (Stations 22 and 57) displayed higher surface Co  
470 uptake rates ( $0.71$  and  $0.51 \text{ pM d}^{-1}$ , respectively, at 25 m depth) than Station 20 in the Ross Sea  
471 ( $0.09 \text{ pM d}^{-1}$  at 30 m depth). It is likely that the lower dCo stoichiometry in Terra Nova Bay was  
472 driven by nutrient draw-down and low availability of labile dCo in the region resulting from  
473 productive phytoplankton blooms. Remineralization would also have played a role in setting the  
474 dCo vs. dPO<sub>4</sub> slope below the photic zone; a remineralization vector with a relatively low slope  
475 indicates that there was a lower dCo source from particulate Co biomass and a rapid turnover of  
476 recycled dCo back into biomass, suggesting a tight coupling of the dissolved and particulate  
477 phases.

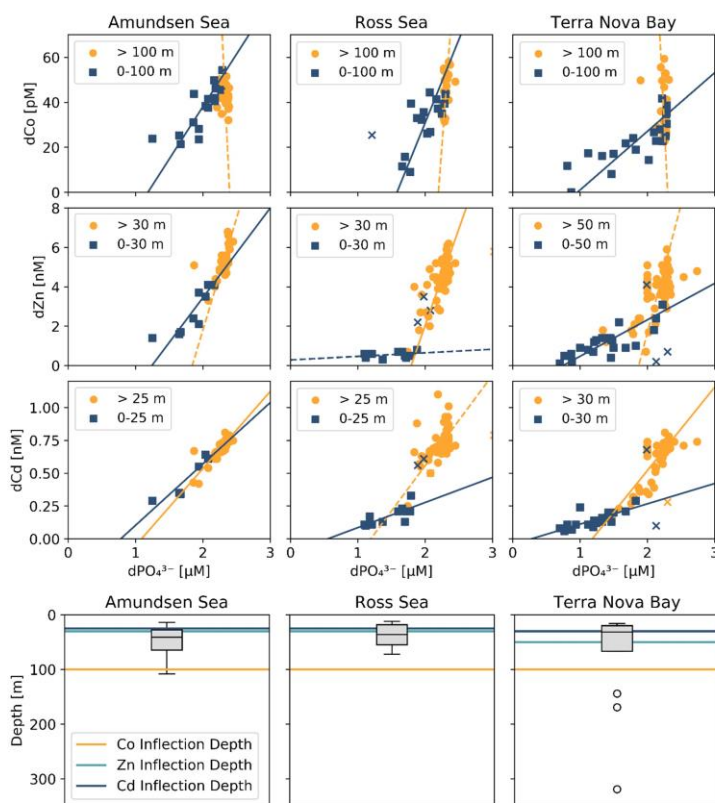




479  
 480 **Figure 6.** (a) A vector schematic of the relationship between  $d\text{PO}_4^{3-}$  and dissolved trace metals  
 481 like dCo, and how the various marine processes can affect their distribution and environmental  
 482 stoichiometry. Adapted from Noble et al. (2008). The CICLOPS (b) dCo vs.  $d\text{PO}_4^{3-}$  relationship  
 483 and (d) labile dCo vs.  $d\text{PO}_4^{3-}$  relationship, plotted by depth. Also shown are the CICLOPS (red)  
 484 (c) dCo vs.  $d\text{PO}_4^{3-}$  and (e) labile dCo vs.  $d\text{PO}_4^{3-}$  samples overlaid with CORSACS (gray) samples.



485



486  
 487 **Figure 7.** (Top 3 rows) Trace metal :  $d\text{PO}_4^{3-}$  relationships from the three CICLOPS regions  
 488 sampled, divided into upper ocean (blue square) and deep ocean (orange circle) bins with a manual  
 489 depth threshold (or inflection point depth) selected to optimize the linear fit of the upper and deep  
 490 ocean trends. Regressions with an  $R^2 \geq 0.50$  are shown as a solid line, and those with an  $R^2 < 0.50$   
 491 are shown as a dotted line. The results of the linear regressions are given in Table 3. Regression  
 492 outliers were selected by hand when including them in the linear regression substantially decreased  
 493 its  $R^2$  value; outliers are marked with an 'x'. (Bottom row) The inflection point depths assigned to  
 494  $d\text{Co}$ ,  $d\text{Zn}$  and  $d\text{Cd}$  relationships are shown compared to a box and whiskers plot of the mixed layer  
 495 depths, with mixed layer depth outliers marked with an 'o'.

496  
 497  
 498  
 499  
 500

501 **Table 3.** Trace metal : dPO<sub>4</sub><sup>3-</sup> stoichiometric regressions for dCo, dZn and dCd in both the surface  
 502 and deep ocean of the Amundsen Sea, Ross Sea and Terra Nova Bay, as shown in Fig. 7. Linear  
 503 regression slopes with R<sup>2</sup> < 0.50 are not shown as the slope values should not be considered  
 504 meaningful stoichiometric values.  
 505

Region	dCo:dPO <sub>4</sub> <sup>3-</sup> [μmol:mol]				dZn:dPO <sub>4</sub> <sup>3-</sup> [mmol:mol]				dCd:dPO <sub>4</sub> <sup>3-</sup> [mmol:mol]			
	Depths [m]	n	Slope	R <sup>2</sup>	Depths [m]	n	Slope	R <sup>2</sup>	Depths [m]	n	Slope	R <sup>2</sup>
<b>Amundsen Sea</b>												
Surface	0-100	16	47 ± 9	0.64	0-30	9	4.6 ± 0.9	0.72	0-25	6	0.47 ± 0.08	0.86
Deep	>100	20	--	0.02	>30	35	--	0.37	>25	38	0.59 ± 0.06	0.72
<b>Ross Sea</b>												
Surface	0-100	15	74 ± 18	0.53	0-30	11	--	0.07	0-25	11	0.19 ± 0.05	0.56
Deep	>100	24	--	0.21	>30	77	9.8 ± 1.0	0.54	>25	79	--	0.26
<b>Terra Nova Bay</b>												
Surf	0-100	20	26 ± 4	0.65	0-50	24	1.9 ± 0.3	0.65	0-30	21	0.15 ± 0.03	0.59
Deep	>100	26	--	0.05	>50	95	--	0.30	>30	104	0.64 ± 0.03	0.80

506  
 507 Deviations from the linear uptake-remineralization line in the dCo vs. dPO<sub>4</sub><sup>3-</sup> relationship  
 508 occur when dCo distributions become decoupled from dPO<sub>4</sub><sup>3-</sup> or vice versa, as with Co scavenging  
 509 onto particles and lithogenic dCo sources. In other ocean regions, the dCo vs. dPO<sub>4</sub><sup>3-</sup> relationship  
 510 displays a characteristic “curl” towards the high- dPO<sub>4</sub><sup>3-</sup>, low-dCo in deeper waters, resulting from  
 511 the net vector sum of both remineralization, which increases both dPO<sub>4</sub><sup>3-</sup> and dCo, and scavenging  
 512 to Mn-oxides, which removes dCo in excess of dPO<sub>4</sub><sup>3-</sup> from the water column (Noble et al., 2008;  
 513 Hawco et al., 2017; Saito et al., 2017). The dCo vs. dPO<sub>4</sub><sup>3-</sup> relationship observed on CICLOPS,  
 514 however, displayed no such scavenging curl, indicating no clear signal of dCo loss due to  
 515 scavenging, at least within timescales relevant to water column mixing. This finding is consistent  
 516 with previous studies of the Ross Sea that have also observed little evidence of dCo loss via  
 517 scavenging in the mesopelagic (Saito et al., 2010; Noble et al., 2013). The lack of a visible  
 518 scavenging signal may be attributable to the deep winter mixed layers of coastal Antarctic seas  
 519 that reach depths of up to 600 m and can extend to the seafloor (Smith and Jones 2015). This deep  
 520 vertical mixing allows the dCo : dPO<sub>4</sub><sup>3-</sup> ratio in the deep ocean to reset on an annual timescale,  
 521 potentially erasing any signals of dCo scavenging, which would be expected to occur on a  
 522 timescale of decades to centuries (Hawco et al., 2017). Additionally, Oldham et al. (2021)  
 523 concluded that a suppressed Co scavenging flux might be the result of a unique Mn cycle in the  
 524 Ross Sea, characterized by low to undetectable concentrations of Mn-oxide particles, slow rates  
 525 of Mn-oxide formation, and the stabilization of organic dMn via Mn(III) ligands (Oldham et al.,  
 526 2021).

#### 527 4.2 Elevated dCo concentrations within a benthic nepheloid layer

528 The elevated dCo signal observed from several depths within 20 m of the seafloor were  
 529 sourced from a benthic nepheloid layer: a near-seafloor region of the water column characterized  
 530 by high particle abundance, turbulence, and isopycnal movement of both dissolved and particulate  
 531 material along the seafloor (Gardner et al., 2018). The Ross Sea has been observed to display  
 532 strong nepheloid layers as cold, dense water flows northward along the Ross Sea shelf until it  
 533 reaches the shelf break, carrying suspended sediments with it along the seafloor (Budillon et al.,  
 534 2006). Nepheloid layers tend to be enriched in dissolved trace metals like dFe, and can act as a  
 535 source of micronutrients if upwelled to the surface ocean (Marsay et al., 2014; Noble et al., 2017).  
 536 Elevated dCo concentrations within the Ross Sea nepheloid layer is a novel finding, as previous

Formatted: Space Before: 12 pt, After: 6 pt

Formatted: Indent: First line: 0.5"

537 expeditions analyzing dCo concentrations in the Ross Sea did not sample as close to the seafloor  
538 as the CICLOPS trace metal rosette was able to (Fitzwater et al., 2000; Saito et al., 2010; Noble et  
539 al., 2013). This finding is evidence of a dCo source to the deep ocean that may be upwelled to  
540 intermediate and upper ocean waters via vertical mixing.

#### 541 4.3.2 Decreased Ross Sea dCo and labile dCo inventories

542 The dCo and labile dCo profiles observed along the 2017/2018 CICLOPS expedition  
543 displayed similar vertical structure as those observed along the 2005/2006 CORSACS expeditions;  
544 however, the CICLOPS dCo and labile dCo concentrations were notably lower throughout the  
545 water column compared to the CORSACS datasets (Fig. 8). This trend was particularly clear in  
546 the Ross Sea, where the stations from both expeditions contained the greatest regional overlap  
547 (Fig. A1) and labile dCo distributions from the prior 2006 CORSACS-2 expedition exceeded those  
548 observed on the 2017/2018 CICLOPS expedition (Fig. 9a-c; Table 4). The CORSACS-1 and  
549 CORSACS-2 expeditions displayed average deep ( $\geq 100$  m) dCo concentrations of  $55 \pm 4$  pM and  
550  $56 \pm 6$  pM, respectively, and CORSACS-2 displayed average deep labile dCo concentrations of  
551  $21 \pm 7$  pM; on CICLOPS, in contrast, the Ross Sea displayed average deep dCo and labile dCo  
552 concentrations of  $46 \pm 8$  pM and  $9 \pm 7$  pM, respectively. Note that the CICLOPS expedition mean  
553 deep dCo inventory displayed a higher standard deviation (8 pM) compared to the CORSACS-1  
554 (4 pM) and CORSACS-2 (6 pM) expeditions, indicating a higher variability of deep dCo  
555 concentration within the sites and depths sampled; no difference in standard deviation was  
556 observed within the deep labile dCo inventories of the CICLOPS and CORSACS-2 expeditions  
557 (both 7 pM). Independent t-tests determined that CORSACS-1 and CORSACS-2 deep Ross Sea  
558 dCo values were statistically similar ( $p = 0.27$ ) while deep CICLOPS dCo values were statistically  
559 different from CORSACS-1 and CORSACS-2 deep dCo ( $p < 0.0001$ ; Table 4). This offset  
560 represents a mean dCo inventory loss of 8 – 10 pM dCo in the deep ocean, and approximately all  
561 of the difference can be accounted for by the loss of deep labile dCo (12 pM dCo; Fig. 9d-g), the  
562 more bioavailable form of dCo for biological uptake. Since a plot of temperature vs. salinity shows  
563 largely overlapping hydrography among the three expeditions in the Ross Sea (Fig. A2), the  
564 observed difference in dCo inventories is unlikely to be due to differences in the distributions of  
565 the water masses sampled.

566 **Table 4.** The mean dCo and labile dCo observed in the deep ( $\geq 100$  m) Ross Sea, and the average  
567 deep dCo loss between 3 previous sampling expeditions (CORSACS-1 in summer 2005/2006;  
568 CORSACS-2 in spring 2006; under-ice sampling in McMurdo Sound in spring 2009) and the  
569 CICLOPS expedition (2017/2018). Dissolved Co and labile dCo loss values were calculated as the  
570 difference between mean deep concentrations observed on previous expeditions and those  
571 observed on the CICLOPS expedition. No labile dCo data (n.d.) is presented from the CORSACS-  
572 1 expedition. Independent t-tests were performed to determine the significance of difference  
573 between the deep mean concentrations from previous expeditions compared to the CICLOPS  
574 expedition; \* indicates a significant difference between CICLOPS and a previous expedition ( $p <$   
575  $0.005$ ). The mean deep dCo concentrations from the CORSACS expeditions were not significantly  
576 different from each other ( $p = 0.27$ ).

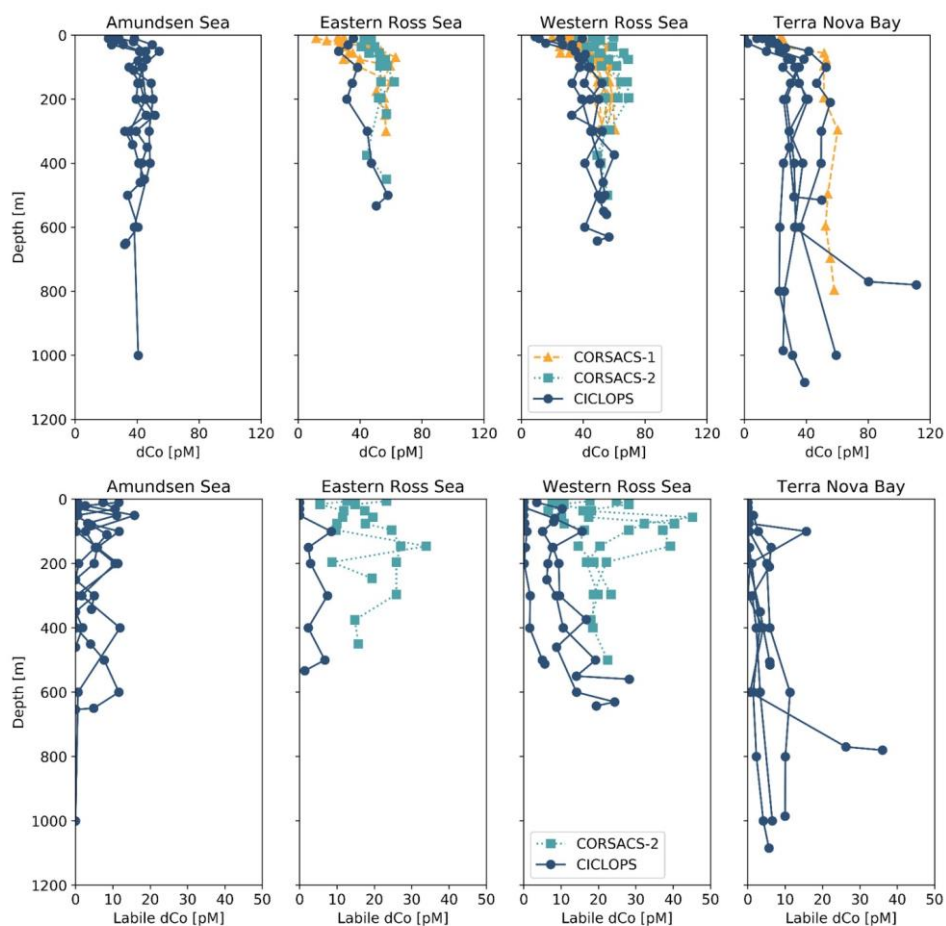


	$dCo_{mean}$ [pM]	n	Labile $dCo_{mean}$ [pM]	n	$dCo$ Loss [pM]	<i>p</i> -value	Labile $dCo$ Loss [pM]	<i>p</i> -value
CORSACS-1 <sup>a</sup>	55 ± 4	26	n.d.		8 ± 9	< 0.0001*	--	--
CORSACS-2 <sup>a</sup>	56 ± 6	19	21 ± 7	20	10 ± 10	< 0.0001*	12 ± 10	< 0.0001*
McMurdo Sound <sup>b</sup>	51 ± 4	19	15 ± 2	19	4 ± 8	0.02	6 ± 7	0.0006*
CICLOPS	46 ± 8	32	9 ± 7	32	--	--	--	--

577

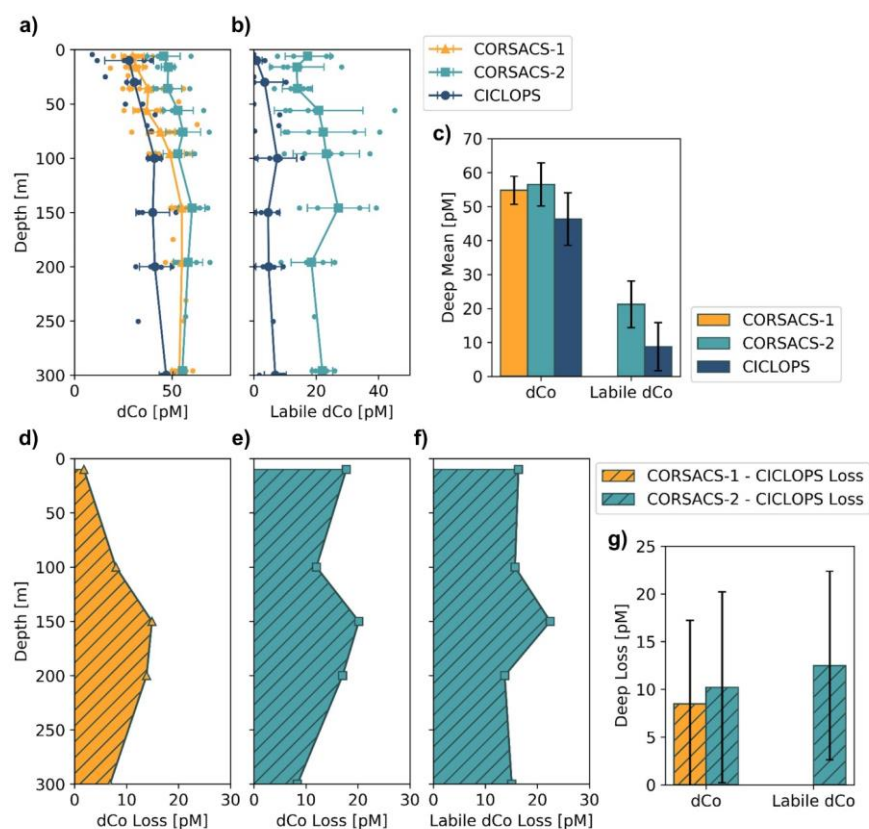
578 <sup>a</sup> Data originally published in Saito et al. (2010).

579 <sup>b</sup> Data originally published in Noble et al. (2013).



580 **Figure 8.** Dissolved Co and labile dCo depth profiles from the CORSACS-1 (NBP0601;  
581 December 27, 2005 – January 23, 2006), CORSACS-2 (NBP0608; November 8, 2006 – December  
582 3, 2006) and CICLOPS (NBP-1801; December 11, 2017 – March 3, 2018) expeditions in the 4

584 regions sampled by the CICLOPS expedition: Terra Nova Bay, the Western Ross Sea, the Eastern  
 585 Ross Sea and the Amundsen Sea. The Eastern and Western Ross Sea stations are defined by being  
 586 either east or west of the 175 °E longitudinal, respectively. The CORSACS expeditions did not  
 587 extend to the Amundsen Sea, and no labile dCo was reported from the CORSACS-1 expedition.  
 588 dCo data from the CORSACS expeditions was reported in Saito et al. (2010) and is accessible at  
 589 <https://www.bco-dmo.org/dataset/3367>.



590 **Figure 9.** Mean depth profiles of dCo (a) and labile dCo (b) from the Ross Sea from three sampling  
 591 seasons, including the expeditions: CORSACS-1 (Summer 2005/2006), CORSACS-2 (Spring  
 592 2006) and CICLOPS (Summer 2017/2018). Observed profile values are plotted as unconnected  
 593 dots, and the mean profile is plotted for each depth at which at least three samples were analyzed.  
 594 (c) The mean deep ( $\geq 100$  m) dCo and labile dCo concentrations for stations in the Ross Sea on  
 595 each expedition. The mean difference in the dCo (d, e) and labile dCo (f) profiles between the  
 596 CORSACS and CICLOPS expeditions where sample depths were within 5 m of each other. (g)  
 597 The mean deep ( $\geq 100$  m) dCo and labile dCo concentration loss for stations in the Ross Sea. Error  
 598 bars denote one standard deviation from the mean. No labile dCo data is available for the  
 599

600 CORSACS-1 expedition. Mean values, loss values, and the results of independent t-tests to  
601 determine the significance of the deep dCo loss are given in Table 4.

602 In the near-surface (10 m), labile dCo was undetectable at 3 of the 4 stations in the Ross  
603 Sea on CICLOPS, and the near-surface labile : total dCo ratio in the one station where labile dCo  
604 was detectable (station 29; 3.5 pM labile dCo) was only 0.09. In contrast, the 2006 CORSACS-2  
605 expedition reported the presence of labile dCo at five stations with concentrations of  $17 \pm 7$  pM at  
606 6 m depth and  $14 \pm 9$  pM at 16 m depth, ~~with~~ reported labile : total dCo ratios ~~at 6 m and 16 m~~  
607 ~~depth~~ of  $0.37 \pm 0.13$  and  $0.28 \pm 0.17$ , respectively. This trend can be at least partially explained by  
608 the seasonality differences between the spring CORSACS-2 expedition and the summer CICLOPS  
609 expedition; as the phytoplankton bloom progresses in the photic zone of the Ross Sea, labile dCo  
610 concentrations would be drawn down by community uptake and would exhibit lower  
611 concentrations later in the summer season. This seasonal trend was evident in the surface dCo  
612 inventory differences between the summer CORSACS-1 and spring CORSACS-2 expeditions  
613 (Fig. 9a,d,e). However, the low, often undetectable, labile dCo concentrations observed in the  
614 surface Ross Sea on the CICLOPS expedition illustrate the intensity of bloom-driven labile dCo  
615 depletion in the region, leaving 91–100% strong ligand-bound dCo in the surface Ross Sea. These  
616 observations are consistent with the Co uptake rate measurements, which were found to be higher  
617 on CICLOPS ( $0.84 \text{ pM d}^{-1}$ ,  $n = 38$ ) compared to CORSACS-1 and CORSACS-2 ( $0.67 \text{ pM d}^{-1}$  and  
618  $0.25 \text{ pM d}^{-1}$ , respectively) (Saito et al., 2010; Rao, 2020).

619 Dissolved Co and labile dCo concentrations were also analyzed in the Ross Sea in 2009 by  
620 sampling the water column below the McMurdo Sound seasonal sea ice in the early spring  
621 (November 9–23) (Noble et al., 2013). Under the ice, the water column was well-mixed, and the  
622 dCo and labile dCo profiles showed relative uniformity at all three stations measured (Fig. 2 of  
623 Noble et al., 2013). In the deep ocean ( $\geq 100$  m), the mean dCo and labile dCo concentrations  
624 were  $51 \pm 4$  and  $15 \pm 2$  pM, respectively, which is lower than those observed on the 2005/2006  
625 CORSACS expeditions and higher than those observed on the 2017/2018 CICLOPS expedition  
626 (Table 4). The mean deep labile dCo concentrations from the McMurdo Sound fieldwork were  
627 also significantly different from the mean deep labile dCo observed on CICLOPS ( $p = 0.0006$ ),  
628 displaying an average deep labile dCo difference of 6 pM. This dataset supports the possibility of  
629 a long-term trend towards a decreasing deep dCo inventory in the Ross Sea, although the more  
630 coastal location and difference in sea ice cover should be considered when comparing the  
631 McMurdo Sound dataset to the CORSACS and CICLOPS observations. Notably, the methodology  
632 and instrumentation used to measure both dCo and labile dCo on both CORSACS expeditions, the  
633 McMurdo Sound fieldwork and the CICLOPS expedition were functionally identical, with the  
634 exception of an autosampler (Metrohm 858 Sample Processor) used on the 2017/2018 CICLOPS  
635 expedition.

636 The low labile dCo inventory in the Ross Sea was a surprising discovery during CICLOPS  
637 since relatively high concentrations of labile dCo were previously noted to be a distinctive feature  
638 of the Ross Sea and Southern Ocean when compared to the tropical and subtropical global oceans  
639 (Saito et al., 2010). In prior studies in this region, high labile : total dCo ratios were hypothesized  
640 to be due to the absence of ligand-producing – and vitamin B<sub>12</sub>-producing – marine cyanobacteria  
641 like *Synechococcus* in the Ross Sea (Caron et al., 2000; DiTullio et al., 2003; Bertrand et al., 2007),  
642 since *Synechococcus*-dominated communities have been known to produce a substantial amount  
643 of Co ligands (Saito et al., 2005). However, high Co ligand concentrations and low labile dCo  
644 concentrations have previously been observed at a more pelagic location in the Southern Ocean

645 near New Zealand, where it was hypothesized that the decay of a eukaryotic phytoplankton bloom  
646 generated higher abundances of Co-binding ligands in the surface ocean (Ellwood et al., 2005).

647 The decrease in the dCo and labile dCo inventories was apparent when the CICLOPS and  
648 CORSACS dCo vs.  $\text{dPO}_4^{3-}$  relationships across all expedition regions were compared (Fig. 6c,e).  
649 Over similar  $\text{dPO}_4^{3-}$  ranges, the CICLOPS dCo concentrations are generally lower than those  
650 observed on CORSACS, and the CICLOPS labile dCo concentrations are considerably lower, with  
651 labile dCo essentially absent from upper ocean samples with a  $\text{dPO}_4^{3-}$  concentration  $< 1.75 \mu\text{M}$ .  
652 Despite the lack of observable scavenging, the CICLOPS dCo vs.  $\text{dPO}_4^{3-}$  relationship appeared to  
653 be noticeably nonlinear throughout the water column ( $R^2 = 0.42$ ), while CORSACS samples  
654 displayed a more linear trend ( $R^2 = 0.57$ ). The CICLOPS dCo vs.  $\text{dPO}_4^{3-}$  relationship creates a  
655 concave, “scooped” shape where dCo was depleted relative to  $\text{dPO}_4^{3-}$ , displaying a lower slope in  
656 the upper ocean than was observed on the CORSACS expeditions (Fig. 6c). This scooped shape  
657 was particularly evident in Terra Nova Bay where the upper ocean dCo :  $\text{dPO}_4^{3-}$  stoichiometric  
658 slope was the lowest ( $26 \pm 4 \mu\text{mol} : \text{mol}$ ;  $R^2 = 0.65$ ). The depletion of dCo relative to  $\text{dPO}_4^{3-}$   
659 observed on CICLOPS appears driven by the shift in Co speciation as a result of near-total uptake  
660 of the upper ocean labile dCo fraction and subsequent dominance of the remaining strong ligand-  
661 bound dCo fraction in the upper ocean. Similar to the deep dCo loss described above, the difference  
662 between the CORSACS and CICLOPS dCo vs.  $\text{dPO}_4^{3-}$  relationship can be accounted for by the  
663 depletion of the labile dCo inventory. In the deep ocean where both dCo and  $\text{dPO}_4^{3-}$  are more  
664 abundant, the large range in dCo concentrations relative to  $\text{dPO}_4^{3-}$  concentrations may be evidence  
665 of deep inputs of dCo and labile dCo from the nepheloid layer, which was more attentively sampled  
666 on CICLOPS than either CORSACS expedition (Sect. 4.1).

#### 667 4.4.3 Dissolved Co, Zn and Cd stoichiometry

668 Dissolved Zn concentrations observed on CICLOPS were low in the surface ocean,  
669 particularly in Terra Nova Bay, where dZn concentrations in the sub-nanomolar ranges were  
670 observed (average dZn =  $0.87 \pm 0.42$  at 10 m depth,  $n = 11$ ). Marine microbes require Zn for a  
671 wide range of metabolic uses; for example, eukaryotic phytoplankton use Zn as a cofactor in  
672 carbonic anhydrase (Roberts et al., 1997; Morel et al., 2020) and bacteria such as  
673 *Pseudoalteromonas* use Zn in a range of proteases (Mazzotta et al., 2021). Prior culture studies  
674 have found that Zn scarcity can lead to co-limitation of both Zn and carbon in several eukaryotic  
675 phytoplankton strains (Morel et al., 1994; Sunda and Huntsman, 2000), and field incubation  
676 experiments have shown evidence for Zn co-limitation with Fe (Jakuba et al., 2012) and silicate  
677 (Chappell et al., 2016) in the Pacific Ocean. During the CICLOPS expedition, an incubation  
678 experiment performed at Station 27 in Terra Nova Bay found compelling evidence for Zn and Fe  
679 co-limitation, which constrained Chl-a production and DIC draw-down by phytoplankton in the  
680 region (Kellogg et al., [Submitted]).

681 Many but not all phytoplankton are able to substitute Co and Cd for Zn as their carbonic  
682 anhydrase metallic cofactor (Lee and Morel, 1995; Sunda and Huntsman, 1995; Lane et al., 2005;  
683 Kellogg et al., 2022), which provides metabolic flexibility and a competitive edge in low-dZn  
684 environments (Kellogg et al., 2020). The Cd-containing carbonic anhydrase CDCA is currently  
685 the only known metabolic use of Cd, and the uptake of dCd and dCo in the photic zone, both metals  
686 which are typically less abundant than dZn in the oceans, often increases under low dZn conditions  
687 (Sunda and Huntsman, 1995, 1996; Jakuba et al., 2008; Kellogg et al., 2020; Morel et al., 2020).  
688 Cations like Zn, Cd and Co that possess similar charge and atomic radii often share the same

689 transporter uptake systems, and the relative availability of different metal cofactors for use in an  
 690 organism's metalloproteome is partially determined by the environmental metal concentrations  
 691 and the affinity of the metals for ligands associated with a cell's metal transport proteins (Irving  
 692 and Williams, 1948; Sunda and Huntsman, 1992, 1995). When dZn concentrations are low, more  
 693 Cd and Co are able to bind to the transporter ligands despite the relative stability of their ligand-  
 694 bound complexes, which tend to be lower for Co than for Zn. Through this mechanism, dZn  
 695 concentrations and cycling can influence the distribution and uptake of Co and Cd, particularly in  
 696 low dZn environments like the Ross Sea and Terra Nova Bay.

697 The dZn vs.  $d\text{PO}_4^{3-}$  and dCd vs.  $d\text{PO}_4^{3-}$  relationships observed in the Amundsen Sea, Ross  
 698 Sea and Terra Nova Bay were compared relative to dCo vs.  $d\text{PO}_4^{3-}$  (Fig. 7; Table 3). For this  
 699 analysis, the depth threshold that separates the upper ocean from the deep ocean was selected  
 700 manually in order to optimize the linear fit of the upper and deep ocean trends and to best capture  
 701 the depth dependence of the observed trace metal stoichiometries. This depth threshold can best  
 702 be conceptualized as an inflection point that represents the largest change in trace metal  
 703 concentrations with respect to depth or, in this case,  $d\text{PO}_4^{3-}$  concentration. The depth threshold  
 704 used for dCo in both the Ross Sea and Terra Nova Bay (100 m) is deeper than those used for dZn  
 705 and dCd, (range of 25 – 50 m). Thus, the inflection points of the “scoops” in the trace metal  
 706 stoichiometries are driven by the uptake stoichiometry of the region's phytoplankton community  
 707 rather than the mixed layer depth of the upper ocean.

708 The ~~resulting shapes of these relationships~~ shapes observed in the dZn vs.  $d\text{PO}_4^{3-}$  and dCd  
 709 vs.  $d\text{PO}_4^{3-}$  relationships were similar to that of dCo vs.  $d\text{PO}_4^{3-}$ , exhibiting distinct differences in  
 710 slope between surface and deep waters. The stark difference in trace metal stoichiometry slopes  
 711 between the upper and deep ocean is likely driven by differences in metal speciation over depth.  
 712 In the surface ocean, a shallower trace metal :  $d\text{PO}_4^{3-}$  slope suggests a trace metal fraction that is  
 713 largely bound to strong organic ligands, with a smaller excess labile fraction. The more  
 714 bioavailable labile fraction of metals would have been drawn down by phytoplankton, whose  
 715 uptake transport systems preferentially bind to labile metals. At deeper depths, the presence of  
 716 labile metals in excess of strong organic ligands results in a higher metal :  $d\text{PO}_4^{3-}$  slope. ~~For this~~  
 717 ~~analysis, the depth threshold that separates the upper ocean from the deep ocean was selected~~  
 718 ~~manually in order to optimize the linear fit of the upper and deep ocean trends and to best capture~~  
 719 ~~the depth dependence of the observed trace metal stoichiometries. This depth threshold can best~~  
 720 ~~be conceptualized as an inflection point that represents the largest change in trace metal~~  
 721 ~~concentrations with respect to depth or, in this case,  $d\text{PO}_4^{3-}$  concentration. The depth threshold~~  
 722 ~~used for dCo in both the Ross Sea and Terra Nova Bay (100 m) is deeper than those used for dZn~~  
 723 ~~and dCd, (range of 25 – 50 m). Thus, the inflection points of the “scoops” in the trace metal~~  
 724 ~~stoichiometries are driven by the uptake stoichiometry of the region's phytoplankton community~~  
 725 ~~rather than the mixed layer depth of the upper ocean.~~

726 A shallow dCo :  $d\text{PO}_4^{3-}$  slope that extends below the photic zone could suggest Co uptake  
 727 by heterotrophic bacteria, archaea and possibly sinking phytoplankton below the photic zone.  
 728 Heterotrophic prokaryotic uptake of labile Co is largely driven by the bacteria and archaea that  
 729 contain a vitamin B<sub>12</sub> synthesis pathway that is absent in all eukaryotes (Warren et al., 2002;  
 730 Osman et al., 2021); unlike carbonic anhydrase, the use of Co as a co-factor in the vitamin B<sub>12</sub>  
 731 corrin ring structure cannot be substituted for by other divalent cations like Zn and Cd. Many  
 732 vitamin B<sub>12</sub>-synthesizing bacteria possess genes for Co(II)-specific transporters in addition to more  
 733 general metal ion transporters, and the Co-specific transporters are regulated by cellular

734 concentrations of vitamin B<sub>12</sub>, illustrating the importance of vitamin B<sub>12</sub> synthesis in driving  
735 bacterial Co uptake (Osman et al., 2021); however, this mechanism has not been observed within  
736 marine bacterial communities. Additionally, vitamin B<sub>12</sub> uptake by both prokaryotes and  
737 eukaryotes has been found to be common in Antarctic coastal communities (Taylor and Sullivan,  
738 2008; Rao, 2020), and likely contributes to the depletion of ligand-bound dCo in both the surface  
739 and mesopelagic ocean.

740 The shallower Zn apparent nutricline could also be explained by the higher stability of Zn  
741 metal-ligand complexes compared to Co complexes within phytoplankton metabolisms, allowing  
742 higher uptake rates of dZn when available (Irving and Williams, 1948; Sunda and Huntsman,  
743 1995). The vertical dimension of trace metal loss captured by a comparison of these apparent  
744 nutriclines could be conceptualized as a time-dependent process driven by the phytoplankton  
745 community's preference for each trace metal, with preferred nutrients like Zn exhibiting a  
746 shallower stoichiometric inflection point arising from the rapid depletion of the metal within the  
747 photic zone, and nutrients like dCo, which is often taken up by eukaryotes when dZn is scarce  
748 (Sunda and Huntsman, 1995; Kellogg et al., 2020), exhibiting a deeper stoichiometric inflection  
749 point below the photic zone. This analysis suggests that substitution at the interface of the uptake  
750 mechanism for trace metal transporters at least partially controlled the stoichiometry of Zn/Cd/Co  
751 distributions and uptake in the upper ocean.

#### 752 4.5.4 Zn/Cd/Co uptake using a shared trace metal membrane transport system

753 This study synthesized dissolved concentration and uptake datasets for Co, Zn and Cd  
754 (Table 5), three trace metal nutrients whose use by phytoplankton is collectively integral to surface  
755 ocean productivity and the biogeochemical cycling of Fe, vitamin B<sub>12</sub> and carbon in the Southern  
756 Ocean. This combined dataset is ideal for interrogating questions of environmental competitive  
757 inhibition of Zn, Cd and Co transport in low-dZn environments. The observation of order of  
758 magnitude trends in trace metal uptake rates over depth profiles ( $\rho\text{Zn} > \rho\text{Cd} > \rho\text{Co}$ ) was novel,  
759 and paralleled the order of magnitude trends of trace metal concentrations in seawater ( $[\text{Zn}] > [\text{Cd}]$   
760  $> [\text{Co}]$ ; Fig 5). This environmental observation reflected the findings of numerous culture  
761 experiments that quantify the uptake of trace metals as a function of the concentration of available  
762 labile metals and the affinity of the metal for a cell transporter's binding ligand (Irving and  
763 Williams, 1948; Sunda and Huntsman, 1992, 1995, 2000; Kellogg et al., 2020).

764 **Table 5.** Dissolved stoichiometric ratios and uptake stoichiometric ratios of five station profiles  
765 for Co, Cd and Zn. The dCo : dCd : dZn : dPO<sub>4</sub><sup>3-</sup> ratio is the dissolved stoichiometry of metals  
766 present in the water column normalized to dPO<sub>4</sub><sup>3-</sup>, and the  $\rho\text{Co} : \rho\text{Cd} : \rho\text{Zn}$  ratio is the uptake  
767 stoichiometry of microbial communities normalized to  $\rho\text{Co}$ .

<b>Region</b>	<b>Station</b>	<b>Depth [m]</b>	<b>dCo : dCd : dZn : dPO<sub>4</sub><sup>3-</sup></b>	<b>ρCo : ρCd : ρZn</b>
Amundsen Sea	4	10	19 : 314 : 1,716 : 1,000,000	1 : 8 : 56
		30	23 : 295 : 1,889 : 1,000,000	1 : 16 : 88
		50	24 : 293 : 2,096 : 1,000,000	1 : 15 : 108
	11	10	13 : 204 : 1,018 : 1,000,000	1 : 10 : 77
		20	15 : 212 : 970 : 1,000,000	1 : 13 : 89
		30	17 : 231 : 1,290 : 1,000,000	1 : 29 : 294
		50	19 : 280 : 1,835 : 1,000,000	1 : 0* : 229
		75	21 : 301 : 2,009 : 1,000,000	1 : 0* : 532
		100	23 : 358 : 2,727 : 1,000,000	1 : 11 : 708
		150	17 : 313 : 1,974 : 1,000,000	1 : 0* : 797
200	17 : 325 : 2,137 : 1,000,000	1 : 3 : 885		
Ross Sea	20	30	17 : 323 : 1,846 : 1,000,000	1 : 13 : 349
		50	13 : 305 : 2,020 : 1,000,000	1 : 11 : 163
		100	17 : 333 : 2,400 : 1,000,000	1 : 0* : 376
		150	16 : 330 : 2,321 : 1,000,000	1 : 0* : 507
		200	14 : 336 : 2,358 : 1,000,000	1 : 0* : 913
Terra Nova Bay	22	10	15 : 136 : 617 : 1,000,000	1 : 12 : 81
		25	10 : 158 : 546 : 1,000,000	1 : 11 : 75
		40	11 : 254 : 1,127 : 1,000,000	1 : 29 : 166
		75	13 : 301 : 1,965 : 1,000,000	1 : 7 : 228
		100	11 : 304 : 1,938 : 1,000,000	1 : 56 : 705
	57	150	16 : 310 : 2,212 : 1,000,000	1 : 122 : 584
		50	13 : 179 : 894 : 1,000,000	1 : 17 : 37
		75	13 : 297 : 1,644 : 1,000,000	1 : 3 : 18
		100	15 : 320 : 1,798 : 1,000,000	1 : 8 : 40

Region	Station	Depth [m]	dCo : dCd : dZn : dPO <sub>4</sub> <sup>3-</sup>	$\rho$ Co : $\rho$ Cd : $\rho$ Zn
Amundsen Sea	4	10	19 : 314 : 1,716 : 1,000,000	1 : 8 : 56
		30	23 : 295 : 1,889 : 1,000,000	1 : 16 : 88
		50	24 : 293 : 2,096 : 1,000,000	1 : 15 : 108
	11	10	13 : 204 : 1,018 : 1,000,000	1 : 10 : 77
		20	15 : 212 : 970 : 1,000,000	1 : 13 : 89
		30	17 : 231 : 1,290 : 1,000,000	1 : 29 : 294
		50	19 : 280 : 1,835 : 1,000,000	1 : 0* : 229
		75	21 : 301 : 2,009 : 1,000,000	1 : 0* : 532
		100	23 : 358 : 2,727 : 1,000,000	1 : 11 : 708
		150	17 : 313 : 1,974 : 1,000,000	1 : 0* : 797
		200	17 : 325 : 2,137 : 1,000,000	1 : 3 : 885
Ross Sea	20	30	17 : 323 : 1,846 : 1,000,000	1 : 13 : 349
		50	13 : 305 : 2,020 : 1,000,000	1 : 11 : 163
		100	17 : 333 : 2,400 : 1,000,000	1 : 0* : 376
		150	16 : 330 : 2,321 : 1,000,000	1 : 0* : 507
		200	14 : 336 : 2,358 : 1,000,000	1 : 0* : 913
Terra Nova Bay	22	10	15 : 136 : 617 : 1,000,000	1 : 12 : 81
		25	10 : 158 : 546 : 1,000,000	1 : 11 : 75
		40	11 : 254 : 1,127 : 1,000,000	1 : 29 : 166
		75	13 : 301 : 1,965 : 1,000,000	1 : 7 : 228
		100	11 : 304 : 1,938 : 1,000,000	1 : 56 : 705
		150	16 : 310 : 2,212 : 1,000,000	1 : 122 : 584
	57	50	13 : 179 : 894 : 1,000,000	1 : 17 : 37
		75	13 : 297 : 1,644 : 1,000,000	1 : 3 : 18
		100	15 : 320 : 1,798 : 1,000,000	1 : 8 : 40

769

770

\*Denotes depths at which  $\rho$ Cd was under the methodological detection limit.

771 Evidence for elevated Co uptake in the low-dZn environments of the surface ocean were  
 772 supported by the trace metal uptake rates. When  $\rho$ Zn and  $\rho$ Cd was normalized to  $\rho$ Co ( $\rho$ TM :  $\rho$ Co;  
 773 Fig. 5), deviations from these order-of-magnitude trends were observed. In particular, at Stations  
 774 4 and 11 in the Amundsen Sea and Station 22 in Terra Nova Bay,  $\rho$ Zn and  $\rho$ Cd stoichiometry  
 775 relative to  $\rho$ Co tended to decrease towards the surface in the upper 50 m, while the opposite trend  
 776 appeared to occur at Station 57 in the late summer. The surface-most trends of stations 20 and 57  
 777 were undetermined due to a lack of a 10 m  $\rho$ Co value. This increasing surface Co uptake  
 778 stoichiometry relative to Zn and Cd at Stations 4, 11 and 22 – stations that also displayed  
 779 significant phytoplankton blooms – suggests that Co uptake increased in low-Zn environments,  
 780 while later in the summer at Station 57,  $\rho$ Co lessened relative to  $\rho$ Zn, possibly due to the deepening  
 781 of the mixed layer in February, bringing additional dZn to the upper ocean via vertical mixing  
 782 (Fig. 4). The increase in the observed  $\rho$ Co rate was likely due to the upregulation of the shared Zn  
 783 and Co uptake transporter system.

784 From laboratory culture experiments aimed at examining the microbial uptake of Zn and  
 785 other trace metals, it is apparent that many diatoms and coccolithophores contain two distinct Zn  
 786 uptake systems: a low-affinity system that operates at higher concentrations of dZn and a high-  
 787 affinity system that functions at lower concentrations of dZn (Sunda and Huntsman, 1992; John et



788 al., 2007). Both transport mechanisms are relatively unspecific as to the divalent metals transported  
 789 into the cell; the low-affinity system is known to transport Zn, Cd and Mn, while the high-affinity  
 790 system transports Zn, Cd and Co. (Sunda and Huntsman, 1995, 1996); thus, Co uptake is often  
 791 inhibited at high dZn concentrations when the low-affinity system is active (Sunda and Huntsman,  
 792 1995; Sunda 2012). In culture, diatoms have been observed to switch from the low-affinity to the  
 793 high-affinity transport system between  $10^{-10.5}$  and  $10^{-9.5}$  M  $dZn^{2+}$  (Sunda and Huntsman, 1992;  
 794 John et al., 2007), a relevant range for the lowest values of total dZn observed in the surface ocean  
 795 on CICLOPS (dZn minimum =  $1 \times 10^{-10}$  M at Station 46, 10 m depth), and the  $dZn^{2+}$  pool would  
 796 have been even smaller due to organic complexation.

797 To investigate the influence of transporter competitive inhibition on trace metal uptake via  
 798 the high-affinity uptake system, we can estimate the predicted  $\rho Co$ ,  $\rho Cd$  and  $\rho Zn$  values given the  
 799 observed trace metal concentrations with an equation adapted from Michaelis-Menten enzyme-  
 800 substrate kinetics (Sunda and Huntsman, 1996, 2000):

$$801 \quad \text{Predicted } \rho M = \frac{V_{\max} [M^{2+}] K_M}{[Co^{2+}] K_{Co} + [Cd^{2+}] K_{Cd} + [Zn^{2+}] K_{Zn}}$$

802 where  $M$  is the trace metal (Co, Cd, Zn) whose uptake is being calculated,  $V_{\max}$  is the saturation  
 803 uptake rate of the transporter system, and  $K_{Co}$ ,  $K_{Cd}$  and  $K_{Zn}$  are steady state affinity constants for  
 804 the metal-ligand complex associated with the membrane transporter. For this system, we assumed  
 805  $K_{Zn} = K_{Cd} = K_{Co} = 10^{9.6}$ , where  $10^{9.6}$  is the value of  $K_{Zn}$  for the high-affinity uptake system  
 806 determined by Sunda et al. (1992), and that 99% of the dCo, dCd and dZn inventory was bound to  
 807 strong organic ligands, leaving 1% of the total metal concentration labile. Note that the assumption  
 808 that  $K$  and the percent labile multipliers are equal for all metals results in their value being nullified  
 809 by their presence in both the numerator and denominator of the predicted uptake equation, and so  
 810 their assumed values have no numerical impact on the predicted uptake values. It was also assumed  
 811 that  $V_{\max}$  values for each trace metal were equal, which is likely a reasonable assumption for metals  
 812 that share an uptake system, although  $V_{\max}$  is known to vary with trace metal concentration, a  
 813 function that we have assumed here to be negligible (Sunda and Huntsman, 1985, 1996; Sunda,  
 814 1989).  $V_{\max}$  is in units of  $\mu\text{mol (mol C)}^{-1} \text{ d}^{-1}$ , and the predicted trace metal uptake rates were  
 815 converted to units of  $\text{M d}^{-1}$  using a C : Chl-a ratio of 130 w/w, derived from the Ross Sea  
 816 phytoplankton community (DiTullio and Smith, 1996).

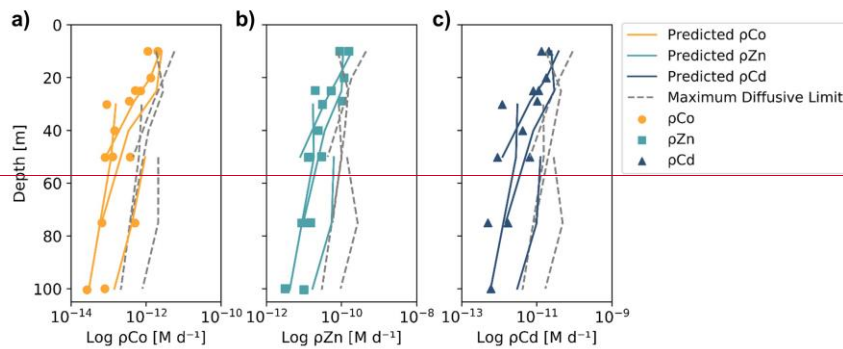
817 When the predicted metal uptake rates were calculated using a  $V_{\max}$  value of 262  $\mu\text{mol (mol C)}^{-1} \text{ d}^{-1}$   
 818 from previous Zn culturing experiments (Sunda and Huntsman, 1992), the resulting values  
 819 recreated the trend of the observed trace metal uptake profiles, with higher uptake rates in the  
 820 surface ocean and lower rates below the photic zone, but the predicted values were over an order  
 821 of magnitude greater than the measured uptake rates (Fig. B.A1). This offset may be due to several  
 822 factors: (1) the assumed C : Chl-a ratio to scale predicted uptake with observed biomass may be  
 823 high, (2) the  $V_{\max}$  value calculated from laboratory experiments may be high, or (3) the  
 824 assumptions that the speciation of the dissolved trace metals are 99% strongly-bound at all depths,  
 825 for all metals is incorrect. The final explanation may play a role in the offset between the predicted  
 826 and observed uptake rates, and illustrates the complexities of translating lab-based culture work to  
 827 environmental measurements and in-situ analyses. The  $V_{\max}$  value is also relatively unconstrained,  
 828 and it is reasonable to assume it may be lower in the Ross Sea than observed in culture if the  
 829 phytoplankton exhibit suppressed metal quotas to survive in a metal-deplete environment. With  
 830 this in mind, the  $V_{\max}$  value was tuned to 4  $\mu\text{mol (mol C)}^{-1} \text{ d}^{-1}$  to fit the observed uptake rates,

831 which is lower than any Co, Cd or Zn  $V_{\max}$  reported in the literature from culture studies (Fig. 10).  
 832 Using the tuned  $V_{\max}$  value, the high-affinity uptake system equation properly predicts the order  
 833 of magnitude trends inherent in the observed Co/Cd/Zn uptake rates. This analysis demonstrates  
 834 the measured uptake rates from the Ross Sea were likely driven by the concentration ratios of  
 835 available metals throughout the water column, following a high-affinity transporter model of Co,  
 836 Cd and Zn uptake.

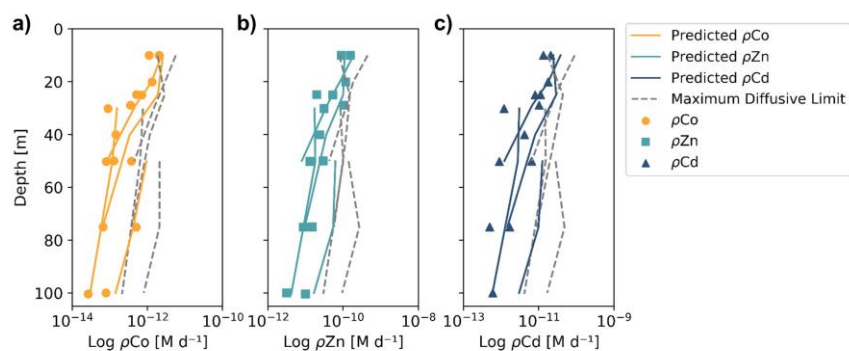
837 The maximum diffusive limit, a calculation of the phytoplankton community's maximum  
 838 diffusion rate for the uptake of trace metal nutrients through their cell membranes, was also  
 839 estimated and compared to the observed and predicted uptake rate profiles. The physical limits of  
 840 uptake via diffusion was determined as a function of the surface area of phytoplankton membranes  
 841 (Sunda and Huntsman, 1992):

$$842 \quad \text{Maximum diffusive limit} = 4\pi r D [M^{2+}]$$

843 where  $r$  is the equivalent spherical radius of a phytoplankton cell, assumed to be 3  $\mu\text{m}$ , a reasonable  
 844 value for diatom species, and  $D$  is a diffusion rate constant of  $2 \times 10^{-6} \text{ cm}^2 \text{ s}^{-1}$ , calculated for  $\text{Zn}^{2+}$   
 845 at 20°C (Sunda and Huntsman, 1992). The diffusive limit was converted to units of  $\text{M d}^{-1}$  using a  
 846 C : cell volume ratio of  $12.5 \text{ mol C L}^{-1}$ , which is the average of two diatom ratios reported in Sunda  
 847 and Huntsman (1995) (11 and 14  $\text{mol C L}^{-1}$ ), and the same C : Chl-a ratio of 130 w/w used for the  
 848 predicted uptake rate estimate above (DiTullio and Smith, 1996). The resulting diffusive limit  
 849 profiles are highly dependent on the assumed speciation of each trace metal; when the dCo, dCd  
 850 and dZn inventories were assumed to be 99% bound (Fig. 10), the maximum diffusive limit was  
 851 slightly greater than the predicted and observed uptake rates, but when the inventories were  
 852 assumed to be 100% labile (Fig. [BA1](#)), the diffusive limit greatly exceeded the uptake rates by  
 853 several orders of magnitude. Since the metal inventories almost certainly vary in their speciation  
 854 of dZn and dCd over depth, as was observed in the dCo inventory, an accurate maximum diffusive  
 855 limit would exist between the two extremes of 0% bound and 99% bound, and might be expected  
 856 to be greater at deeper depths, where a higher fraction of the dissolved metal inventory is labile.  
 857 For additional analysis of the predicted metal uptake ratios and the maximum diffusive limit, see  
 858 Appendix [BH](#).



859



Formatted: Centered

860  
 861 **Figure 10.** Observed (markers) and predicted (solid lines) trace metal uptake rate ( $\rho$ ) profiles for  
 862 Co (a) Zn (b) and Cd (c) from Stations 11, 20, 22 and 57. The maximum diffusive limit profiles  
 863 (dashed lines) are shown as an estimate of the physical limits of metal diffusion through uptake  
 864 transporters. The predicted uptake rates were tuned to best fit the observed uptake rate trends by  
 865 using a  $V_{\max}$  value of  $4 \mu\text{mol} (\text{mol C}^{-1}) \text{d}^{-1}$ , and the maximum diffusion limit estimation assumed  
 866 a speciation of 0.01% labile metals.

#### 867 4.65 Vitamin B<sub>12</sub> and Zn stress, and their implications for increasing biological dCo demand

868 The near-absence of labile dCo and low concentration of ligand-bound dCo in coastal  
 869 Antarctic seas may indicate a larger shift in the region towards vitamin B<sub>12</sub> limitation. Vitamin B<sub>12</sub>  
 870 has been shown to be co-limiting with Fe in the Ross Sea and elsewhere (Sañudo-Wilhelmy et al.,  
 871 2006; Bertrand et al., 2007), and increased vitamin B<sub>12</sub> uptake by both bacterioplankton and  
 872 eukaryotic phytoplankton has been observed in incubation experiments following the alleviation  
 873 of surface ocean Fe limitation (Bertrand et al., 2011). Two primary sources of Fe to the Antarctic  
 874 seas are a flux of lithogenic Fe from melting ice shelves along the continent and sediment  
 875 resuspension along the seafloor, both of which have been observed to be meaningful Fe sources to  
 876 the Amundsen Sea (Planquette et al., 2013; St-Laurent et al., 2017). The source of particulate Fe  
 877 from glacial meltwater to coastal Antarctic seas has been increasing over the past several decades  
 878 and is expected to continue to increase as Antarctic ice shelves and glaciers melt and retreat due  
 879 to global climate change (Monien et al., 2017). The source of particulate Co from glacial meltwater  
 880 would also be expected to increase since Co, like Fe, has been observed to be transported from the  
 881 Antarctic continent via ice melt (Westerlund and Öhman, 1991), and it is unclear what role this  
 882 presumably increasing source of Co to the surface ocean plays in the reduced inventories of dCo  
 883 in the surface ocean.

884 Although it is difficult to definitively conclude that the low dCo inventory observed on  
 885 CICLOPS is representative of a decadal trend towards vitamin B<sub>12</sub> limitation and not simply  
 886 variation in micronutrient availability and community structure, the inventory and stoichiometric  
 887 uptake trends documented in this study are compelling evidence for a changing biogeochemical  
 888 Co cycle in the coastal Southern Ocean. Paired with the recent discovery of Zn/Fe co-limitation in  
 889 Terra Nova Bay (Kellogg et al., [Submitted]), these results suggest a complex landscape of  
 890 micronutrient scarcity and limitation in coastal Antarctic seas where plankton community

891 structures and Fe additions from melting ice sheets can generate patches of vitamin B<sub>12</sub> and Zn  
892 limitation within a broadly Fe-scarce HNLC region.

893 The bacterial community is essential to the development and alleviation of vitamin B<sub>12</sub>  
894 limitation within a eukaryotic phytoplankton bloom since only prokaryotes possess the metabolic  
895 pathway to synthesize the vitamin (Warren et al., 2002; Croft et al., 2005). In the Southern Ocean,  
896 near-zero counts of photosynthetic bacteria indicate that the heterotrophic bacterial communities  
897 are primarily responsible for vitamin B<sub>12</sub> production in the region (Bertrand et al., 2011). Vitamin  
898 B<sub>12</sub> can become limiting when the bacterial community is low in abundance and/or growth limited  
899 by a different nutrient such as dissolved organic matter (DOM). In the Ross Sea, bacterioplankton  
900 have been found to be growth limited by an inadequate supply of DOM (Church et al., 2000;  
901 Bertrand et al., 2011), and there can be up to a one-month lag between the onset of the spring  
902 phytoplankton bloom and an associated bacterial bloom stimulated by phytoplankton DOM  
903 production (Ducklow et al., 2001). This offset suggests that vitamin B<sub>12</sub> limitation among  
904 eukaryotes is most probable earlier in the season within the spring bloom. Additionally, low  
905 abundances of mesozooplankton and microzooplankton grazing rates in the Ross Sea create  
906 phytoplankton blooms with low grazing pressure (Caron et al., 2000; Ducklow et al., 2001), which  
907 may allow low DOM conditions to persist later into a bloom and exacerbate vitamin B<sub>12</sub> stress  
908 among eukaryotes.

909 A shift towards vitamin B<sub>12</sub> limitation would likely favor phytoplankton with flexible  
910 metabolisms that are able to reduce their demand for Co and vitamin B<sub>12</sub> when necessary.  
911 Organisms that can express the vitamin B<sub>12</sub>-independent *metE* gene may out-compete those  
912 expressing the vitamin B<sub>12</sub>-dependent *metH* gene (Rao et al., [In review]; Rodionov et al., 2003;  
913 Bertrand et al., 2013; Helliwell 2017). *P. antarctica*, for example, may be well suited to periods  
914 of vitamin B<sub>12</sub> limitation due to the symbiotic bacterial microbiomes that form within its colonies  
915 and produce B vitamins that allow the colonies to grow when B vitamins are otherwise unavailable  
916 (Brisbin et al., 2022). *P. antarctica* has also been found to express a novel *metE*-fusion gene when  
917 vitamin B<sub>12</sub> limited and *metH* gene while vitamin-replete, suggesting a highly flexible vitamin B<sub>12</sub>  
918 metabolism (Rao et al., [In review]).

919 There is compelling evidence for high rates of biological Co uptake in the Ross Sea during  
920 the 2017/2018 summer compared to the 2005/2006 summer driven by the uptake of dCo from  
921 vitamin B<sub>12</sub> and Zn scarcity. Together, these two stressors increase the rate of Co uptake as well  
922 as the Co : C stoichiometry of phytoplankton biomass. The stoichiometry of Co uptake has been  
923 observed to be highly plastic in this study and others, responding to the availability of other  
924 micronutrients and the requirements of the microbial community (Sunda and Huntsman, 1995;  
925 Saito et al., 2017). An increase in  $\rho$ Co could then result in a decrease of the Co inventory in coastal  
926 Antarctic seas, following the mechanism detailed below.

927 Biological uptake alone would not permanently remove Co from the water column; uptake  
928 only shifts Co from the dissolved phase to the particulate phase, where POM remineralization  
929 restores Co back to the dissolved phase. The net removal pathways of Co include (1) burial as  
930 POM, (2) particle scavenging and (3) depletion of dCo into Circumpolar Deep Water (CDW) and  
931 Antarctic Bottom Water (ABW). We have already noted that Co scavenging to Mn-oxides is  
932 particularly low in the Southern Ocean (Oldham et al., 2021). The advection of dCo into CDW  
933 may not be at a steady state throughout the year since cycles of ice melt and formation affect the  
934 mixing of CDW and formation of dense Antarctic Bottom Water (ABW), and so may represent a  
935 removal pathway for dCo on an annual cycle. However, an increase in the burial flux of Co in

936 POM is the most likely pathway for sustained loss of the Co inventory. When the  $\rho\text{Co}$  rate  
 937 increases, the stoichiometry of Co incorporation into biomass relative to P would also increase.  
 938 Over the years, a strengthened demand for Co via vitamin B<sub>12</sub> and Zn stress could result in a steady  
 939 loss of Co if the Co : C and Co : PO<sub>4</sub><sup>3-</sup> stoichiometry of POM increases but the remineralization of  
 940 POM is unchanged, increasing the flux of particulate Co into the deep ocean and sediments. In the  
 941 winter, sea ice covers the Antarctic seas and the water column mixes, a process that would  
 942 propagate the low dCo concentrations from the photic zone into the deep ocean and result in a  
 943 steady loss of the dCo inventory throughout the water column.

944 Additionally, warming surface ocean temperatures likely play a role in phytoplankton  
 945 productivity and nutrient uptake. Increasing both dFe availability and temperature have been  
 946 shown to significantly increase phytoplankton growth and phytoplankton abundance in the Ross  
 947 Sea, and impact community structure (Rose et al., 2009; Spackeen et al., 2018; Zhu et al., 2016).  
 948 From a kinetic perspective, higher surface temperatures would be expected to increase the uptake  
 949 rates of nutrients, including micronutrients like Fe, Co and Zn, by increasing the value of  $K_M$ .  
 950 However, the effects of temperature on productivity and community composition are more  
 951 complex since increasing ocean temperatures would also decrease the solubility of CO<sub>2</sub>, change  
 952 the seasonality of ice cover and thus sunlight availability, and affect water column turnover and  
 953 mixing regimes (Rose et al., 2009). The effects of warming temperatures on the intricate landscape  
 954 of nutrient availability and limitation regimes described here is an open question in this study.

#### 955 4.7.6 A two-box model that describes a mechanism for deep dCo inventory loss

956 To test the proposed mechanism that higher Co uptake rates and winter mixing can lead to  
 957 a deep inventory loss of ~10 pM Co over 12 years, a time step two-box model of a 1 m<sup>2</sup> water  
 958 column was created in Microsoft Excel to simulate the Ross Sea dCo cycle. A schematic of the  
 959 modeled dCo cycle is presented in Fig. 11, flux equations to describe the biogeochemical cycling  
 960 of Co are presented in Appendix C4, and the parameters used to simulate dCo loss over 12 years  
 961 and a hypothetical steady state condition are given in Table 6.

962 The change in dCo concentration over time ( $d[\text{dCo}]/dt$ ) for a surface ocean (0–100 m) and  
 963 deep ocean (100–500 m) was calculated as the sum of the dCo source fluxes minus the sum of the  
 964 sink fluxes:

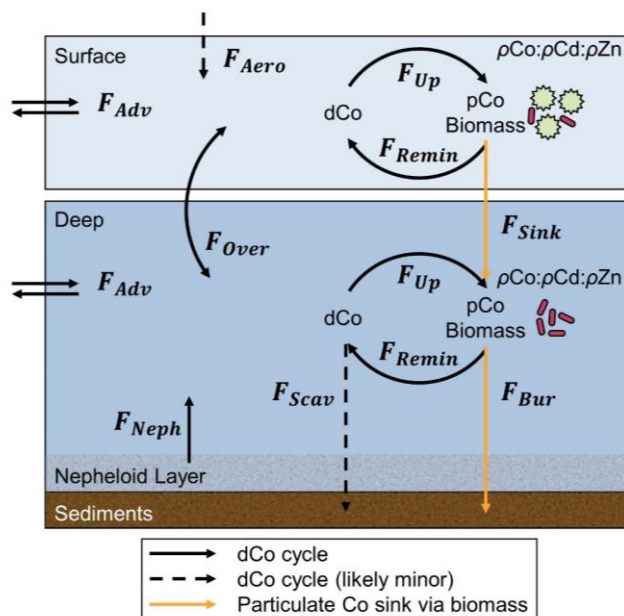
$$965 \left(\frac{d[\text{dCo}]}{dt}\right)_{\text{Surface}} = \frac{F_{\text{Over}} + F_{\text{Remin}} - F_{\text{Up}}}{V_{\text{Surface}}}$$

$$966 \left(\frac{d[\text{dCo}]}{dt}\right)_{\text{Deep}} = \frac{F_{\text{Remin}} + F_{\text{Neph}} - F_{\text{Up}} - F_{\text{Over}}}{V_{\text{Deep}}}$$

967 where  $F_{\text{Over}}$  is the overturning flux between the two boxes,  $F_{\text{Remin}}$  is the remineralization flux,  $F_{\text{Up}}$   
 968 is the biological uptake flux, and  $F_{\text{Neph}}$  is the flux of dCo from the nepheloid layer into the deep  
 969 ocean (Table CB1).  $F_{\text{Up}}$  was calculated using the measured  $\rho\text{Co}$  uptake rates observed on the  
 970 CORSACS and CICLOPS expeditions, and  $F_{\text{Remin}}$  was calculated using an assumed surface and  
 971 deep remineralization factor (RF) of 0.9, indicating that 90% of the POM generated in the surface  
 972 ocean is remineralized back to its inorganic dissolved components. In the Southern Ocean, the  
 973 fluxes of scavenging and aerosol deposition would be relatively negligible, so these fluxes have  
 974 been omitted from the model. The magnitude of  $F_{\text{Neph}}$  in the Ross Sea remains unconstrained, and  
 975 in this model, the deep nepheloid dCo source was used as an adjustable parameter to tune the

Formatted: Font: Italic

976 magnitude of deep dCo loss to be 10 pM over 12 years, which represents the approximate observed  
 977 differences between the CORSACS and CICLOPS expeditions detailed in Sect. 4.3.2. A  $F_{Neph}$  was  
 978 calculated to be 3550 pmol  $dCo \cdot m^{-2} \cdot d^{-1}$  to the deep ocean, but this should not be considered a  
 979 meaningful calculation of the observed nepheloid layer flux.



980 **Figure 11.** A schematic of the dCo cycle (black arrows) and select processes of the particulate Co  
 981 (pCo) cycle (orange arrows) presented as a simplified two-box model. Net fluxes of the dCo cycle  
 982 include sources from aerosol deposition ( $F_{Aero}$ ), bottom sediments and the nepheloid layer ( $F_{Neph}$ ),  
 983 and scavenging to Mn-oxides particles ( $F_{Scav}$ ) which likely represents a minor flux in the coastal  
 984 Antarctic seas. Internal cycling fluxes include horizontal advection ( $F_{Adv}$ ), water column  
 985 overturning or mixing ( $F_{Over}$ ), biological uptake ( $F_{Up}$ ) and remineralization of pCo ( $F_{Remin}$ ). Fluxes  
 986 of pCo shown here include sinking biomass from the surface into the deep ocean ( $F_{Sink}$ ) and pCo  
 987 burial into sediments along the seafloor ( $F_{Bur}$ ). The biological uptake of dCo is influenced by the  
 988 relative stoichiometric uptake of Co, Zn and Cd ( $\rho_{Co} : \rho_{Cd} : \rho_{Zn}$ ) among the microbial  
 989 community. Differential equations that describe and quantify these fluxes are presented in  
 990 Appendix Cf.  
 991

992 In the Ross Sea, the deep winter mixed layer can extend 600 m to the seafloor and turn  
 993 over the whole water column in some locations (Smith and Jones, 2015), mixing the surface and  
 994 deep ocean under the winter sea ice and resulting in near-vertical profiles of dCo in the early spring  
 995 (Noble et al., 2013). Here, the winter mixing process was modeled by combining the surface and  
 996 deep ocean boxes into one homogenized box during the winter season (151 days, ~5 months). The  
 997 dCo concentrations of the winter box were calculated using a volume-weighted average (see  
 998 Appendix Cf).

999 **Table 6.** Parameters of the Co cycle two-box model, run as both a steady state model with lower  
 1000 Co uptake rates ( $\rho\text{Co}$ ) and as a mechanism for deep dCo inventory loss driven by higher  $\rho\text{Co}$   
 1001 values. The calculated burial flux of particulate Co within each model variation is also given, but  
 1002 note that the burial flux values should be interpreted as a comparison of the Co sink via the  
 1003 biological pump when  $\rho\text{Co}$  is varied, and not as observed or meaningful Co flux magnitudes.

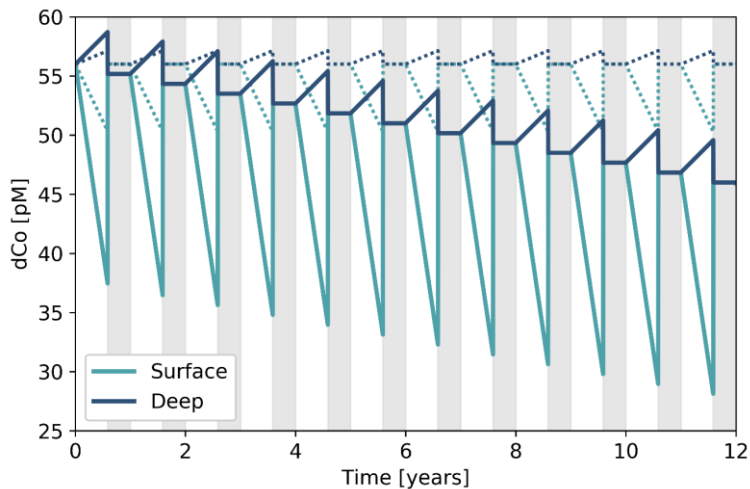
Model Parameters	Value	Units
Bloom season length	214	days
Surface box height	100	m
Deep box height	500	m
Remineralization Factor (RF)	0.9	
Deep Nephloid Flux	3550	$\text{pmol Co m}^{-2} \text{d}^{-1}$
Overturning Water Flux	0	$\text{m}^3 \text{d}^{-1}$
<b>Steady State Parameters</b>		
Surface $\rho\text{Co}$	0.27	$\text{pmol Co L}^{-1} \text{d}^{-1}$
Deep $\rho\text{Co}$	0.66	$\text{pmol Co L}^{-1} \text{d}^{-1}$
Burial Flux	3550	$\text{pmol Co m}^{-2} \text{d}^{-1}$
<b>dCo Loss Parameters</b>		
Surface $\rho\text{Co}$	0.87	$\text{pmol Co L}^{-1} \text{d}^{-1}$
Deep $\rho\text{Co}$	0.1	$\text{pmol Co L}^{-1} \text{d}^{-1}$
Burial Flux	5870	$\text{pmol Co m}^{-2} \text{d}^{-1}$
<b>Model Parameters</b>		
Bloom season length	214	days
Surface box height	100	m
Deep box height	500	m
Remineralization Factor (RF)	0.9	
Deep Nephloid Flux	3550	$\text{pmol Co m}^{-2} \text{d}^{-1}$
Overturning Water Flux	0	$\text{m}^3 \text{d}^{-1}$
<b>Steady State Parameters</b>		
Surface $\rho\text{Co}$	0.27	$\text{pmol Co L}^{-1} \text{d}^{-1}$
Deep $\rho\text{Co}$	0.66	$\text{pmol Co L}^{-1} \text{d}^{-1}$
Burial Flux	3550	$\text{pmol Co d}^{-1}$
<b>Co Loss Parameters</b>		
Surface $\rho\text{Co}$	0.87	$\text{pmol Co L}^{-1} \text{d}^{-1}$
Deep $\rho\text{Co}$	0.1	$\text{pmol Co L}^{-1} \text{d}^{-1}$
Burial Flux	5870	$\text{pmol Co d}^{-1}$

1004

1005

1006 This model provides a plausible mechanism by which increases in  $\rho\text{Co}$  such as those  
 1007 observed along the CICLOPS expedition might increase the burial flux of particulate Co, resulting  
 1008 in a net loss to the deep dCo inventory. The uptake rate of Co both within and below the photic  
 1009 zone, as well as the fraction of POM that is remineralized, dictated the flux of particulate Co into  
 1010 the sediments via burial. The initial dCo concentration was set at 56 pM, which approximates the

1011 mean deep dCo concentrations observed on both CORSACS-1 and CORSACS-2. When the model  
 1012 was run for 12 years, the time period between the first CORSACS expedition and the CICLOPS  
 1013 expedition, it generated a sawtooth pattern; the surface and deep boxes diverged over the course  
 1014 of the summer bloom season as biological uptake removed dCo from the surface box and  
 1015 remineralization replenished dCo in the deep box (Fig. 12). Winter mixing then unified and reset  
 1016 the water column, replenishing the surface dCo inventory. The model was run at a steady state  
 1017 using the average surface  $\rho\text{Co}$  rate observed on CORSACS-1 ( $0.27 \text{ pmol L}^{-1} \text{ d}^{-1}$ ; Table 6) (Saito  
 1018 et al., 2010) and deep  $\rho\text{Co}$  values that were tuned to allow no change in the deep dCo inventory  
 1019 every winter. When the model was run using representative surface and deep  $\rho\text{Co}$  values observed  
 1020 on the CICLOPS expedition ( $0.87$  and  $0.1 \text{ pmol Co L}^{-1} \text{ d}^{-1}$ , respectively), the surface depletion of  
 1021 dCo was more pronounced by the end of the bloom season compared to the steady state model,  
 1022 and winter mixing resulted in a steady annual decrease of the deep dCo inventory. The mechanism  
 1023 of dCo loss was driven by increasing  $\rho\text{Co}$ , particularly in the surface ocean, and the propagation  
 1024 of dCo loss into the deep ocean via vertical mixing. The resulting burial flux when the model  
 1025 exhibited a deep dCo loss mechanism was higher than when the model was run at a steady state  
 1026 (Table 6), demonstrating how higher Co uptake rates among plankton paired with a deep winter  
 1027 mixed layer can result in a diminishing dCo inventory on a decadal timescale.



1028 **Figure 12.** Results of the two-box model illustrating a potential mechanism for the loss of the dCo  
 1029 inventory over time. Gray boxes represent the winter season when the surface and deep boxes mix.  
 1030 The dotted lines represent a system at a steady state, where the dCo inventory stays consistent  
 1031 annually. The solid lines represent a system exhibiting dCo loss, where increased Co uptake rates  
 1032 in both the surface and deep ocean result in an annually decreasing dCo inventory. The initial deep  
 1033 dCo concentration was 56 pM, which approximates the mean deep dCo concentrations observed  
 1034 on CORSACS-1 and CORSACS-2. Over 12 years, the dCo loss model depicts the loss of  $0.83 \text{ pM}$   
 1035  $\text{year}^{-1}$  to end at a deep dCo inventory of 46 pM, the mean deep dCo concentration observed on  
 1036 CICLOPS.  
 1037

1038 The purpose of this model was to illustrate a possible mechanism for a dCo inventory loss  
 1039 over the 12-year period between the CORSACS and CICLOPS expeditions using reasonable



1040 estimates of Co uptake and other Co cycle fluxes to achieve the observed 10 pM deep inventory  
1041 loss. This box model successfully shows the directionality of the changes to the deep ocean dCo  
1042 inventory and deep burial flux when the  $\rho$ Co values increase, but the magnitude of the estimated  
1043 Co burial or the nepheloid Co source should not be considered meaningful flux values. The model  
1044 represented a greatly simplified version of the carbon pump in the Southern Ocean, and it is likely  
1045 that at least some of the unquantified Co cycle fluxes were not negligible, including horizontal  
1046 advection, overturning water during the summer season, Co scavenging, and a surface aerosol  
1047 source. Additionally, it is a simplifying assumption that  $\rho$ Co values would be consistent throughout  
1048 a surface or deep depth region, as well as consistent over an entire summer season. Despite its  
1049 simplicity, the box model presented a concise and reasonable mechanism for this study's  
1050 observation of a shrinking dCo inventory in the Ross Sea.

## 1051 **5 Conclusion**

1052 The Ross Sea, Amundsen Sea and Terra Nova Bay displayed lower dCo and labile dCo  
1053 inventories during the 2017/2018 austral summer relative to prior observations in the region, which  
1054 is consistent with observations of higher rates of Co use and uptake by phytoplankton and  
1055 heterotrophic bacteria. The near-100% complexation of the dCo inventory reveals that the dCo  
1056 loss is primarily due to the uptake of labile dCo, the most bioavailable form of dCo to marine  
1057 microbes. The decrease in dCo throughout the water column compared to prior observations is  
1058 indicative of a multi-year mechanism, whereby the removal of dCo from the surface mixed layer  
1059 via uptake over the summer has been propagated into the deep ocean via winter mixing, resulting  
1060 in a decrease in dCo concentration throughout the water column. This mechanism is reliant upon  
1061 increased dCo uptake into organic matter and an increase in the burial rate of Co as organic matter.  
1062 This change—The observed biogeochemical differences may be due to the alleviation of Fe  
1063 limitation through inputs from increased glacial melting and subsequent development of  
1064 intermittent vitamin B<sub>12</sub> and/or Zn limitation, both of which would be expected to increase the  
1065 demand for Co among plankton communities.

1066 In coastal Antarctica and other regions impacted by global climate change, Co is a  
1067 noteworthy trace metal nutrient to investigate because its small inventory and flexible  
1068 phytoplankton stoichiometry make its biogeochemical cycle particularly vulnerable to  
1069 perturbation. In the Arctic Ocean, for example, the dCo and labile dCo inventories have increased  
1070 as melting ice and permafrost have increased the flux of Co-enriched riverine waters and sediments  
1071 to the upper ocean (Bundy et al., 2020). Like many other trace nutrients, the Co cycle is integrally  
1072 connected to that of other elements like Zn, Cd, Fe and carbon, and observations of perturbed Co  
1073 inventories and changing nutrient limitation regimes would affect their biogeochemical cycles as  
1074 well. In highly productive coastal Antarctic seas, shifts in micronutrient inventories and growth  
1075 limitation could have implications for the composition of regional phytoplankton blooms and the  
1076 magnitude of the Southern Ocean carbon sink.

1077 Since the late 1980s, it has been hypothesized that the primary productivity and net carbon  
1078 sequestration flux of the Southern Ocean is controlled by the supply of Fe to surface waters (Martin  
1079 1990; Martin et al., 1990). This theory, called the “iron hypothesis”, posits that the addition of  
1080 bioavailable Fe to an Fe-limited surface ocean stimulates productivity and, in turn, increases the  
1081 regional and possibly global carbon sequestration flux from the atmosphere into deep ocean  
1082 sediments. When applied to potential carbon dioxide removal (CDR) geoengineering projects, the  
1083 iron hypothesis provides a theoretical framework for ocean iron fertilization (OIF), where

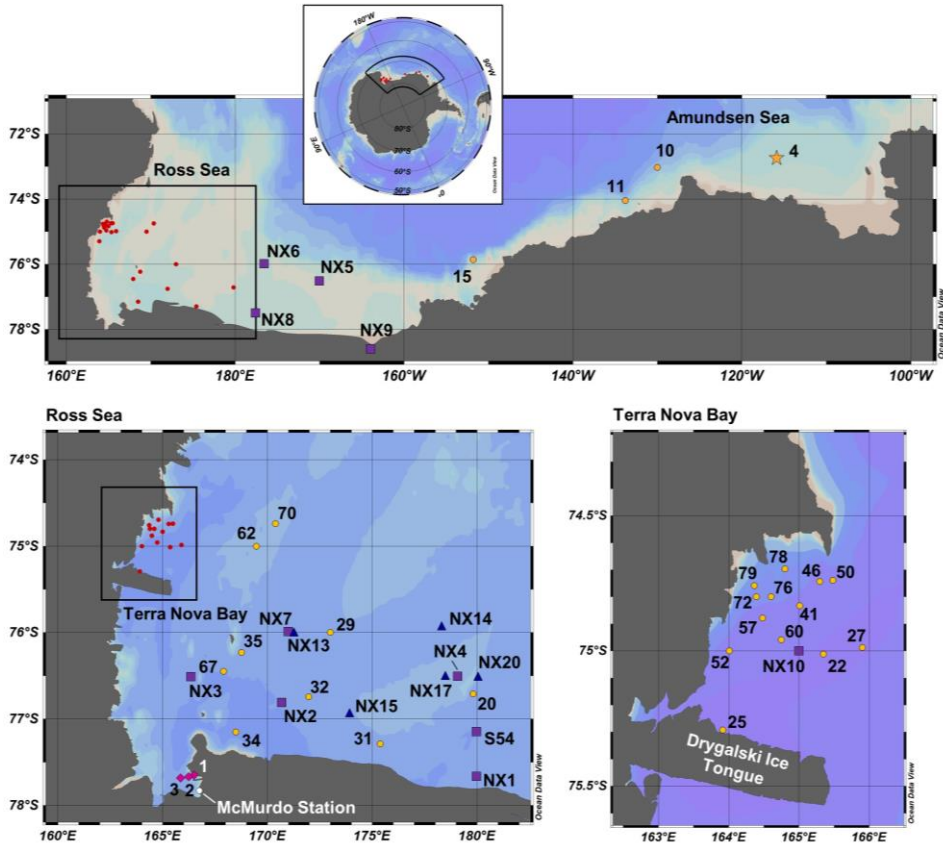
1084 significant quantities of Fe are introduced to the surface Southern Ocean to enhance the net  
1085 sequestration of CO<sub>2</sub> and reduce global atmospheric CO<sub>2</sub> concentrations (Emerson, 2019). Over  
1086 the past three decades, several mesoscale Fe fertilization experiments have shown that large  
1087 phytoplankton blooms can be stimulated by the addition of Fe to the surface Southern Ocean, and  
1088 that the impact on the CO<sub>2</sub> sink is variable, modest and often difficult to assess (Coale et al., 1996;  
1089 Boyd et al., 2000; de Baar et al., 2005; Smetacek et al., 2012). This study provides additional  
1090 insights into the potential of OIF, suggesting that the alleviation of Fe limitation might shift the  
1091 region towards the limitation of another trace nutrient such as vitamin B<sub>12</sub>, Zn, and potentially Co.  
1092 The nutrient limitation regimes of the Southern Ocean are complex, heterogeneous and possibly  
1093 shifting on decadal timescales, and these intricacies must be examined when considering future  
1094 OIF projects.

1095

1096

1097

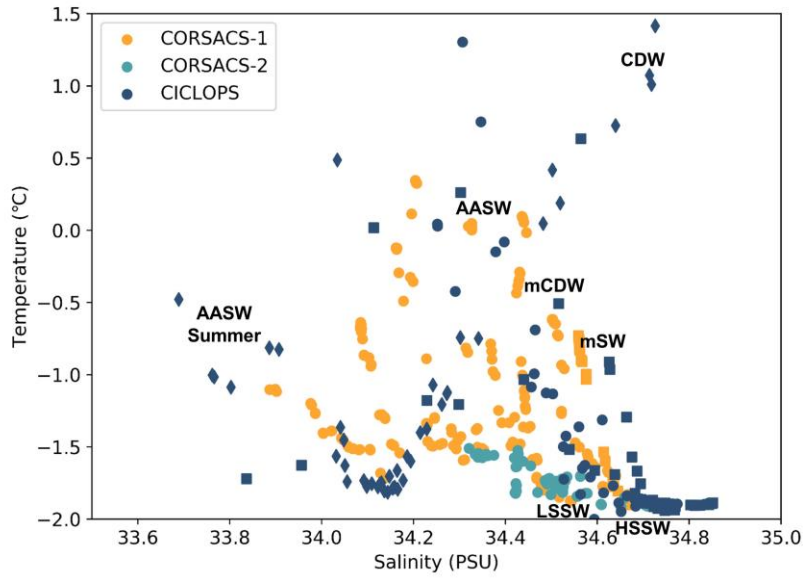
1098 **Appendix A. Locations and hydrography of historical Ross Sea and Terra Nova Bay stations**



Formatted: Centered

099  
100 **Figure A1.** Map of CICLOPS (yellow circles), CORSACS-1 (purple squares), CORSACS-2 (blue  
101 triangles) and McMurdo Sounds fieldwork (magenta diamonds) stations in coastal Antarctic  
102 waters, including insets of stations within the Ross Sea and Terra Nova Bay. Only stations from  
103 the CORSACS-1 and CORSACS-2 expeditions whose data is used in this study are shown.  
104 Stations marked in red are CICLOPS stations shown in more detail in an inset. Note that the grey  
105 coastline marks both terrestrial coastline and areas of consistent ice, including ice shelves and  
106 glaciers; this includes the Drygalski Ice Tongue, a glacier to the south of Terra Nova Bay.

Formatted: Font: Not Bold



Formatted: Centered

108

109

110

111

112

113

114

115

116

117

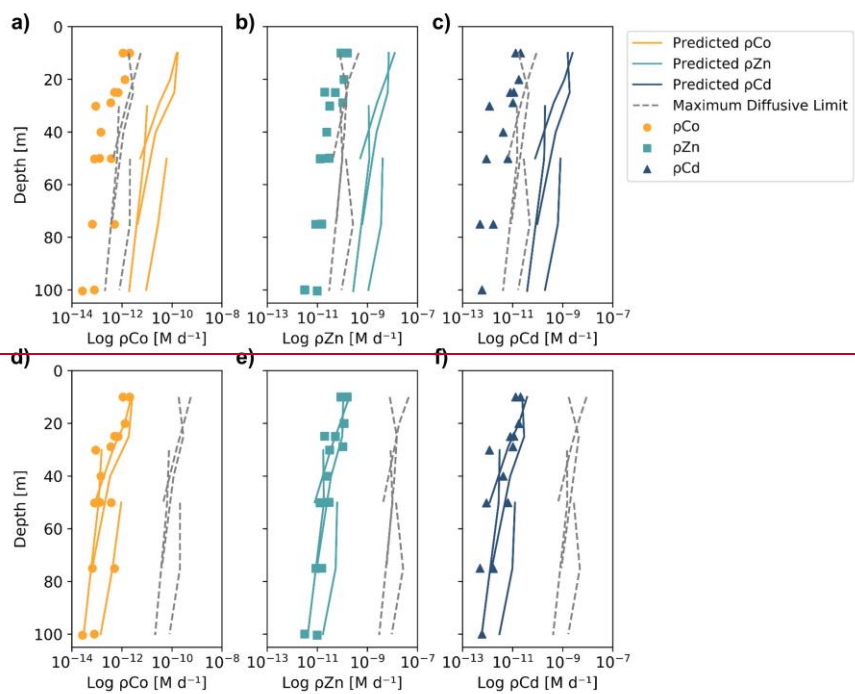
118

**Figure A2.** The Temperature-Salinity relationship and water mass classification of samples from the Amundsen Sea (diamonds), Ross Sea (circles) and Terra Nova Bay (squares). Sample data is shown only from samples used to compare dCo data from the CORSACS-1, CORSACS-2 and CICLOPS expeditions in Sect. 4.3. Labeled water masses include Circumpolar Deep Water (CDW), modified Circumpolar Deep Water (mCDW), modified Shelf Water (mSW), Low Salinity Shelf Water (LSSW), High Salinity Shelf Water (HSSW), Antarctic Surface Water (AASW), and the fresher summertime AASW (AASW Summer). Classification of water mass samples from the CICLOPS expedition are taken from Rao (2020), Figure 3-25 and references therein. Note that the CORSACS-1, CORSACS-2 and CICLOPS expeditions largely overlapped in their water mass distribution in the Ross Sea and Terra Nova Bay.

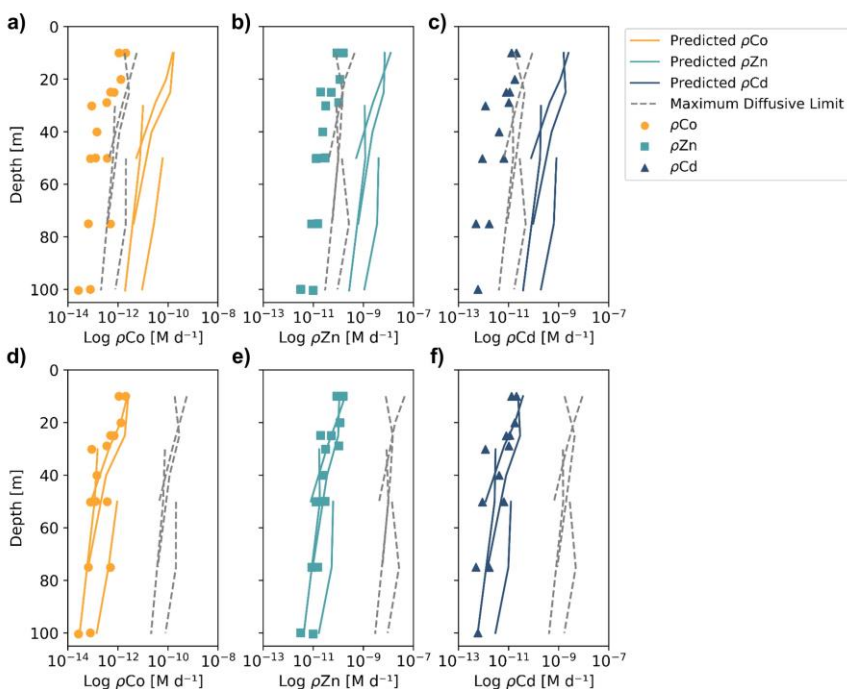
Formatted: Font: Not Bold

Formatted: Font: Not Bold

1119 **Appendix BA.** Estimating trace metal uptake and maximum rate of dissolution profiles from  
 1120 classic competitive inhibition equations.



1121



1122  
 1123 **Figure BA1.** Observed (markers) and predicted (solid lines) trace metal uptake rate ( $\rho M$ ) profiles  
 1124 and the estimated maximum diffusive limit profiles (dashed line) for Co (**a,d**) Zn (**b,e**) and Cd (**c,f**)  
 1125 from Stations 11, 20, 22 and 57, using different equation parameters than those used in Fig. 10. In  
 1126 panels a-c, the predicted uptake rates used a literature  $V_{\max}$  value of  $262 \mu\text{mol} (\text{mol C}^{-1}) \text{d}^{-1}$   
 1127 determined from  $\text{Zn}^{2+}$  uptake experiments in *Emiliania huxleyi* cultures (Sunda and Huntsman,  
 1128 1992), resulting in predicted uptake rates that were orders of magnitude greater than the observed  
 1129 values. In panels d-f, the estimated maximum diffusive limit profiles assumed that 100% of the  
 1130  $d\text{Co}$ ,  $d\text{Zn}$  and  $d\text{Cd}$  inventories were labile and 0% were bound to strong organic ligands, resulting  
 1131 in diffusive limits that were also orders of magnitude greater than the observed values. This  
 1132 analysis helps to show how parameter assumptions can greatly influence the predicted uptake rates  
 1133 and illustrates the difficulty of assigning kinetic parameters to environmental analyses.  
 1134

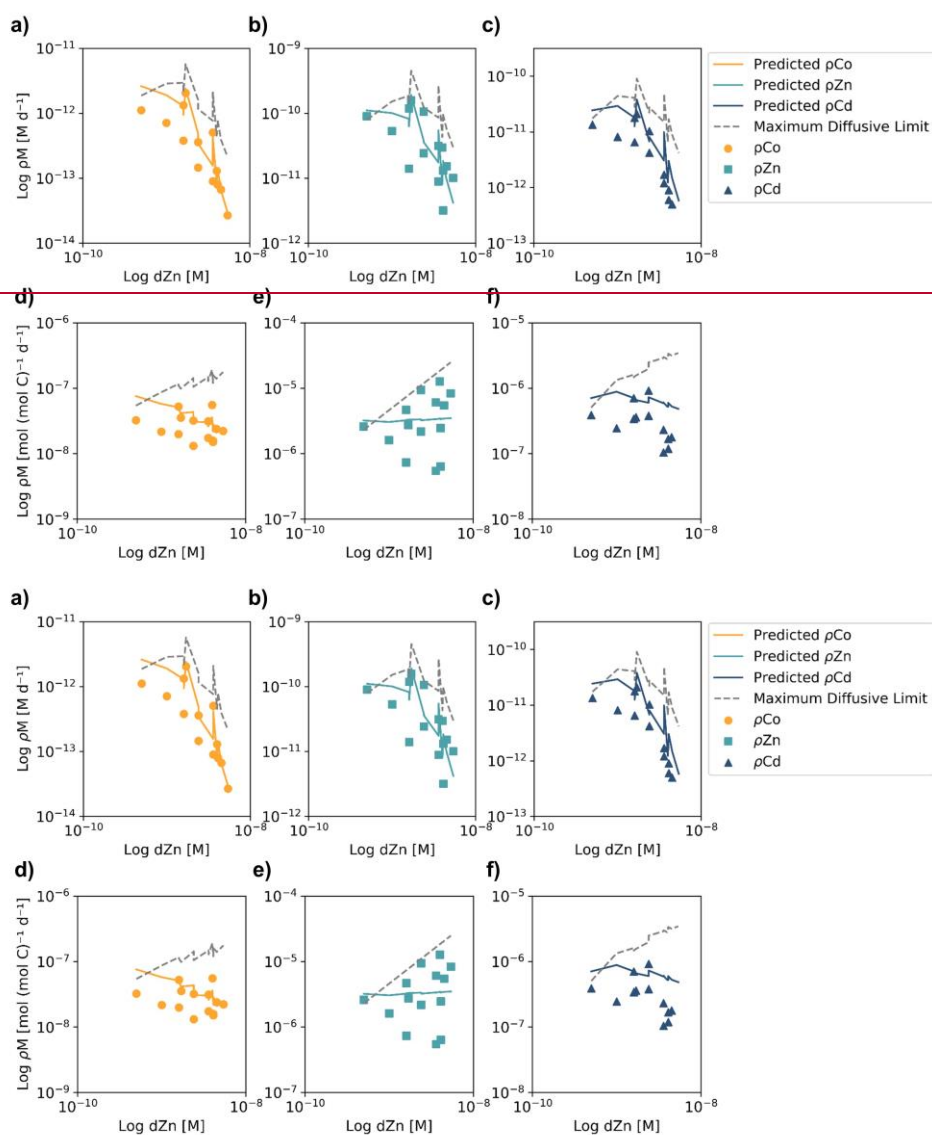


**Figure BA2.** Observed (markers) and predicted (solid lines) trace metal uptake rates ( $\rho\text{M}$ ) and the estimated maximum diffusive limit profiles (dashed line) plotted against total dZn concentrations, assuming a  $V_{\text{max}}$  of  $4 \mu\text{mol (mol C}^{-1} \text{d}^{-1})$  and that 99% of the trace metal inventory was bound to strong organic ligands. Panels a-c show  $\rho\text{M}$  in units of  $\text{M d}^{-1}$ , which tended to decrease at high dZn concentrations. This is attributable to higher dZn concentrations below the photic zone, where

1142 much lower rates of micronutrient uptake occur. Panels **d-f** show  $\rho M$  when normalized to biomass  
1143 using Chl-a concentrations and a C : chl-a ratio of 130 w/w (DiTullio and Smith, 1996). The  
1144 normalized predicted  $\rho Zn$  values are relatively stable over the observed range of dZn  
1145 concentrations, while the predicted  $\rho Co$  and  $\rho Cd$  values decrease slightly as dZn increases,  
1146 suggesting that competitive inhibition of  $\rho Co$  and  $\rho Cd$  may have occurred at higher dZn  
1147 concentrations due to the smaller inventories of dCo and dCd compared to dZn.  
1148



1149 **Appendix CB. Description of a two-box model of the dCo cycle in coastal Antarctic seas, and**  
 1150 **a potential mechanism for deep dCo loss with changing microbial uptake stoichiometry.**

1151 The two-box model described below was used to conceptualize the biogeochemical cycling  
 1152 of dCo in the surface and deep ocean. The model describes a 1 m<sup>2</sup> column of water with a total  
 1153 depth of 600 m and a depth threshold between the surface and deep box of 100 m. Within each  
 1154 box, the net change of dCo over time is equivalent to the sum of the source fluxes minus the sum  
 1155 of the sink fluxes:

$$\left(\frac{d[dCo]}{dt}\right)_{Surface} = \frac{\sum(F_i)_{Sources} - \sum(F_i)_{Sinks}}{V_{Surface}}$$

$$\left(\frac{d[dCo]}{dt}\right)_{Deep} = \frac{\sum(F_i)_{Sources} - \sum(F_i)_{Sinks}}{V_{Deep}}$$

1156 where fluxes ( $F_i$ ) are in units of mols dCo d<sup>-1</sup>. A summary of the sources and sinks relevant to  
 1157 dCo in coastal Antarctic seas is shown below in Table CB1. In the Southern Ocean, we would  
 1158 expect the fluxes of scavenging ( $F_{Scav}$ ) and aerosol deposition ( $F_{Aero}$ ) would be relatively  
 1159 negligible, and so these fluxes have been omitted from the model. Additionally, we can assume  
 1160 that horizontal advection is at a steady state, and thus the net advection flux is  $\approx 0$  mols dCo d<sup>-1</sup>.  
 1161 This gives us the net equations for both boxes:

$$\left(\frac{d[dCo]}{dt}\right)_{Surface} = \frac{F_{Over} + F_{Remin} - F_{Up}}{V_{Surface}}$$

$$\left(\frac{d[dCo]}{dt}\right)_{Deep} = \frac{F_{Remin} + F_{Neph} - F_{Up} - F_{Over}}{V_{Deep}}$$

1166 **Table CB1:** The source and sink fluxes of dCo in the surface and deep ocean boxes. Fluxes are  
 1167 theoretically in units of mols dCo d<sup>-1</sup>.

Surface Sources		Surface Sinks		Deep Sources		Deep Sinks	
Remineralization	$F_{Remin}$	Microbial Uptake	$F_{Up}$	Remineralization	$F_{Remin}$	Microbial Uptake	$F_{Up}$
Overturning	$F_{Over}$	Advection	$F_{Adv}$	Nepheloid Layer	$F_{Neph}$	Overturning	$F_{Over}$
Aerosols	$F_{Aero}$			Advection	$F_{Adv}$	Scavenging	$F_{Scav}$
Advection	$F_{Adv}$					Advection	$F_{Adv}$

1168 Uptake fluxes

1169 The flux of dCo incorporation into microbial biomass via uptake by protein transporters  
 1170 can be described using the uptake rates ( $\rho_{Co}$ ) measured by <sup>57</sup>Co incubation experiments, where  
 1171 units of  $\rho_{Co}$  are in mols dCo L<sup>-1</sup> d<sup>-1</sup>:

$$F_{Up,Surface} = (\rho_{Co,Surface} * V_{Surface})$$

$$F_{Up,Deep} = (\rho_{Co,Deep} * V_{Deep})$$

## 1178 Remineralization fluxes

1179 In this model, the remineralization flux of particulate Co in organic matter to dCo is  
 1180 quantified by a Remineralization Factor (RF), which can be applied to the amount of particulate  
 1181 matter present in each box. Typical RF values tend to be between 0.90 and 0.99 (Glover et al.,  
 1182 2011), meaning that between 90% and 99% of all microbial biomass produced tends to be  
 1183 remineralized before sinking out of its respective box. It is not clear that the RFs for the surface  
 1184 and deep box should be represented by the same value, and so we have defined both surface  
 1185 ( $RF_{Surface}$ ) and deep ( $RF_{Deep}$ ) variables here. In the surface ocean, excess Co in un-remineralized  
 1186 biomass will sink into the deep box ( $F_{Sink}$ ), where it is further able to be remineralized in the deep  
 1187 ocean. In the deep ocean, excess Co in un-remineralized biomass is assumed to flux into the  
 1188 sediments via burial ( $F_{Bur}$ ), representing a key sink of dCo biomass out of the two-box system. The  
 1189 surface box remineralization flux is represented with a relatively simple equation:

$$1190 \quad F_{Remin, Surface} = RF_{Surface} * F_{Up, Surface}$$

$$1191 \quad F_{Remin, Surface} = RF_{Surface} (\rho CO_{Surface} * V_{Surface})$$

1192 The deep ocean remineralization flux can then be calculated as the sum of the  
 1193 remineralization flux from excess biomass that sinks as particulate Co and biomass generated in  
 1194 the deep ocean:

$$1195 \quad F_{Remin, Deep} = RF_{Deep} (F_{Up, Surface} - F_{Remin, Surface}) + RF_{Deep} (F_{Up, Deep})$$

$$1196 \quad F_{Remin, Deep} = RF_{Deep} (\rho CO_{Surface} * V_{Surface} - RF_{Surface} (\rho CO_{Surface} * V_{Surface})) \\ 1197 \quad + RF_{Deep} (\rho CO_{Deep} * V_{Deep})$$

## 1198 Overturning fluxes

1199 An overturning dCo flux represents the flux of a volume of water from the deep ocean box  
 1200 into the shallow ocean box, and a corresponding flux of the same volume from the shallow ocean  
 1201 box into the deep ocean box for mass conservation. In a dynamic coastal upwelling system like  
 1202 the Ross and Amundsen Seas, the reality of this overturning flux is almost certainly much more  
 1203 complicated, as coastal upwelling processes overlap with meltwater processes and deep water mass  
 1204 formation processes. For the purposes of this two-box model, the flux of dCo via overturning can  
 1205 be estimated as a function of the overturning water flux ( $F_{Water}$ ) and the dCo concentrations of each  
 1206 box:

$$1207 \quad F_{Over, Surface} = (F_{Water} [dCo]_{Deep} - F_{Water} [dCo]_{Surface})$$

$$1208 \quad F_{Over, Deep} = (F_{Water} [dCo]_{Surface} - F_{Water} [dCo]_{Deep})$$

1209 In the model presented in Sect. 4.7.6, the  $F_{Water}$  and both  $F_{Over}$  fluxes are assumed to be  
 1210 negligible for the sake of modeling simplicity, but the introduction of a nonzero overturning flux  
 1211 would help to make the seasonal change in the dCo inventory in both the surface and deep oceans  
 1212 nonlinear, as it is currently the only flux in this model that is calculated using the time step's dCo  
 1213 concentrations.

## 1214 Flux from the nepheloid layer

1215 At several CICLOPS stations, a distinct nepheloid layer was detected as dCo concentration  
 1216 increased sharply at depths immediately above (~10 m) the ocean floor. The nepheloid layer tends

1217 to contain high levels of particles moving horizontally along the seafloor, and is likely a significant  
 1218 source of dCo to the surrounding water column. The source of dCo from the nepheloid layer is  
 1219 somewhat unclear; it could be via dissolution of particles suspended within the nepheloid layer or  
 1220 from a porewater flux of dCo out of the sediments. In this model, the flux of deep dCo inputs into  
 1221 the deep ocean, assumed to be from the nepheloid layer, was derived using the Microsoft Excel  
 1222 solver tool, given the parameter that 10 pM of deep dCo was lost over 12 years. The deep source  
 1223 of dCo was calculated to be 3550 pmol dCo m<sup>-2</sup> d<sup>-1</sup>. This value should be considered an adjustable  
 1224 parameter used to tune the model to our conceptual understanding of dCo inventory loss, and not  
 1225 a meaningful calculation of observed Co flux from the deep nepheloid layer, which has yet to be  
 1226 constrained.

1227 The cobalt burial sink

1228 The loss of cobalt from the deep ocean box into the sediments via burial can be quantified  
 1229 with the equation:

$$1230 \left( \frac{d[Co]}{dt} \right)_{Bur} = F_{Sink} + F_{Up,Deep} - F_{Remin,Deep}$$

1231 where  $F_{Sink}$  is described by:

$$1232 F_{Sink} = (\rho Co_{Surface} * V_{Surface}) - RF_{Surface}(\rho Co_{Surface} * V_{Surface})$$

1233 This estimate of the loss of dCo due to burial assumes that all biogenic particulate Co that is not  
 1234 remineralized in the surface ocean sinks into the deep ocean, and all biogenic particulate Co that  
 1235 is not remineralized in the deep ocean is sequestered in sediments and “lost” to the model.

1236 Modeling seasonality: the winter mixed layer

1237 In the Ross and Amundsen Seas, sea ice covers the surface ocean for a larger portion of the  
 1238 year (~ 5 months). During this time, the water column mixes – a process that was modeled by  
 1239 combining the two-box model into one homogenized box after the 7-month bloom season to  
 1240 simulate the winter season. This process can be modeled by a volume-weighted average with the  
 1241 volume of each box.

$$1242 [dCo]_{Winter} = \frac{(V_{Surface} * [dCo]_{Surface}) + (V_{Deep} * [dCo]_{Deep})}{(V_{Surface} + V_{Deep})}$$

#### 1243 Data availability

1244 The CICLOPS dCo dataset has been submitted to the Biological and Chemical Oceanography Data  
 1245 Management Office (BCO-DMO) website (<https://www.bco-dmo.org/project/774945>) and is  
 1246 pending approval for publication. The dissolved metals (dZn, dCd) dataset (<https://www.bco-dmo.org/dataset/877466>),  
 1247 Zn and Cd uptake rate dataset (<https://www.bco-dmo.org/dataset/877681>), and macronutrient dataset (<https://www.bco-dmo.org/dataset/874841>)  
 1248 are publicly available on the BCO-DMO website.  
 1249

#### 1250 Author contribution

1251 RC collected and analyzed dCo samples and wrote the manuscript. RK collected and analyzed  
 1252 dZn and dCd samples and measured Zn and Cd uptake rates. DR measured Co uptake rates. GD

1253 collected and analyzed phytoplankton pigment samples. All authors assisted in the collection and  
1254 processing of dissolved seawater samples and incubation experiment samples, and all authors  
1255 helped write the manuscript.

#### 1256 **Competing interests**

1257 The authors declare that they have no conflict of interest.

#### 1258 **Acknowledgments**

1259 The authors thank the captain, crew and science party of the RVIB *Nathaniel B. Palmer* for their  
1260 support during the CICLEPS expedition. We also thank Joe Jennings (OSU) for dissolved  
1261 macronutrient analysis, Véronique Oldham for sampling assistance, and Matthew Charette,  
1262 Stephanie Dutkiewicz, and Alessandro Tagliabue for writing insights. This work was funded by  
1263 grants from the National Science Foundation's Office of Polar Programs (OPP-1643684, OPP-  
1264 1644073 and OPP-1643845).

#### 1265 **References**

- 1266 Arrigo, K. R., Robinson, D. H., Worthen, D. L., Dunbar, R. B., DiTullio, G. R., Vanwoert, M.  
1267 and Lizotte, M. P.: Phytoplankton community structure and the drawdown of nutrients and CO<sub>2</sub>  
1268 in the Southern Ocean, *Science*, 283, 365–367, 1999.
- 1269 Arrigo, K. R., van Dijken, G. L. and Bushinsky, S.: Primary production in the Southern Ocean,  
1270 1997-2006, *J. Geophys. Res.*, 113, C08004, doi:10.1029/2007JC004551, 2008.
- 1271 Arrigo, K. R., Lowry, K. E. and van Dijken, G. L.: Annual changes in sea ice and phytoplankton  
1272 in polynyas of the Amundsen Sea, Antarctica, *Deep. Res. Part II Top. Stud. Oceanogr.*, 71–76,  
1273 5–15, doi:10.1016/j.dsr2.2012.03.006, 2012.
- 1274 de Baar, H. J. W., Boyd, P. W., Coale, K. H., Landry, M. R., Tsuda, A., Assmy, P., Bakker, D.  
1275 C. E., Bozec, Y., Barber, R. T., Brzezinski, M. A., Buesseler, K. O., Boyé, M., Croot, P. L.,  
1276 Gervais, F., Gorbunov, M. Y., Harrison, P. J., Hiscock, W. T., Laan, P., Lancelot, C., Law, C. S.,  
1277 Levasseur, M., Marchetti, A., Millero, F. J., Nishioka, J., Nojiri, Y., van Oijen, T., Riebesell, U.,  
1278 Rijkenberg, M. J. A., Saito, H., Takeda, S., Timmermans, K. R., Veldhuis, M. J. W., Waite, A.  
1279 M. and Wong, C. S.: Synthesis of iron fertilization experiments: From the iron age in the age of  
1280 enlightenment, *J. Geophys. Res. C Ocean.*, 110(9), 1–24, doi:10.1029/2004JC002601, 2005.
- 1281 Bernhardt, H. and Wilhelms, A.: The continuous determination of low level iron, soluble  
1282 phosphate and total phosphate with the AutoAnalyzer(TM), in *Technicon Symposium*, vol. 1, p.  
1283 386., 1967.
- 1284 Bertrand, E. M., Saito, M. A., Rose, J. M., Riesselman, C. R., Lohan, M. C., Noble, A. E., Lee,  
1285 P. A. and DiTullio, G. R.: Vitamin B12 and iron colimitation of phytoplankton growth in the  
1286 Ross Sea, *Limnol. Oceanogr.*, 52(3), 1079–1093, doi:10.4319/lo.2007.52.3.1079, 2007.
- 1287 Bertrand, E. M., Saito, M. A., Lee, P. A., Dunbar, R. B., Sedwick, P. N. and DiTullio, G. R.: Iron  
1288 limitation of a springtime bacterial and phytoplankton community in the Ross Sea: implications  
1289 for vitamin B12 nutrition, *Front. Microbiol.*, 2, 160, doi:10.3389/fmicb.2011.00160, 2011.
- 1290 Bertrand, E. M., Moran, D. M., McIlvin, M. R., Hoffman, J. M., Allen, A. E. and Saito, M. A.:  
1291 Methionine synthase interreplacement in diatom cultures and communities: Implications for the

- 1292 persistence of B12 use by eukaryotic phytoplankton, *Limnol. Oceanogr.*, 58(4), 1431–1450,  
1293 doi:10.4319/lo.2013.58.4.1431, 2013.
- 1294 Bown, J., Boye, M. and Nelson, D. M.: New insights on the role of organic speciation in the  
1295 biogeochemical cycle of dissolved cobalt in the southeastern Atlantic and the Southern Ocean,  
1296 *Biogeosciences*, 9, 2719–2736, doi:10.5194/bg-9-2719-2012, 2012.
- 1297 Boyd, P. W., Watson, A. J., Law, C. S., Abraham, E. R., Trull, T., Murdoch, R., Bakker, D. C.  
1298 E., Bowie, A. R., Buesseler, K. O., Chang, H., Charette, M., Croot, P., Downing, K., Frew, R.,  
1299 Gall, M., Hadfield, M., Hall, J., Harvey, M., Jameson, G., LaRoche, J., Liddicoat, M., Ling, R.,  
1300 Maldonado, M. T., McKay, R. M., Nodder, S., Pickmere, S., Pridmore, R., Rintoul, S., Safi, K.,  
1301 Sutton, P., Strzepek, R., Tanneberger, K., Turner, S., Waite, A. and Zeldis, J.: A mesoscale  
1302 phytoplankton bloom in the polar Southern Ocean stimulated by iron fertilization, *Nature*,  
1303 407(6805), 695–702, doi:10.1038/35037500, 2000.
- 1304 Brisbin, M. M., Mitarai, S., Saito, M. A. and Alexander, H.: Microbiomes of bloom-forming  
1305 *Phaeocystis* algae are stable and consistently recruited, with both symbiotic and opportunistic  
1306 modes, *ISME J*, doi:10.1038/s41396-022-01263-2, 2022.
- 1307 Budillon, G., Salusti, E. and Tucci, S.: The evolution of density currents and nepheloid bottom  
1308 layers in the Ross Sea (Antarctica), *J. Mar. Res.*, 64(4), 517–540,  
1309 doi:10.1357/002224006778715739, 2006.
- 1310 Bundy, R. M., Tagliabue, A., Hawco, N. J., Morton, P. L., Twining, B. S., Hatta, M., Noble, A.,  
1311 Cape, M. R., John, S. G., Cullen, J. T. and Saito, M. A.: Elevated sources of cobalt in the Arctic  
1312 Ocean, *Biogeosciences*, 17, 4745–4767, doi:https://doi.org/10.5194/bg-2020-84, 2020.
- 1313 Caron, D. A., Dennett, M. R., Lonsdale, D. J., Moran, D. M. and Shalapyonok, L.:  
1314 Microzooplankton herbivory in the Ross Sea, Antarctica, *Deep Sea Res. II*, 47, 3249–3272,  
1315 2000.
- 1316 Chandler, J. W., Lin, Y., Gainer, P. J., Post, A. F., Johnson, Z. I. and Zinser, E. R.: Variable but  
1317 persistent coexistence of *Prochlorococcus* ecotypes along temperature gradients in the ocean's  
1318 surface mixed layer, *Environ. Microbiol. Rep.*, 8(2), 272–284, doi:10.1111/1758-2229.12378,  
1319 2016.
- 1320 Chappell, P. D., Vedmati, J., Selph, K. E., Cyr, H. A., Jenkins, B. D., Landry, M. R. and Moffett,  
1321 J. W.: Preferential depletion of zinc within Costa Rica upwelling dome creates conditions for  
1322 zinc co-limitation of primary production, *J. Plankton Res.*, 38(2), 244–255,  
1323 doi:10.1093/plankt/fbw018, 2016.
- 1324 Chmiel, R., Lanning, N., Laubach, A., Lee, J.-M., Fitzsimmons, J., Hatta, M., Jenkins, W. J.,  
1325 Lam, P. J., Mcilvin, M., Tagliabue, A. and Saito, M. A.: Major processes of the dissolved cobalt  
1326 cycle in the North and equatorial Pacific Ocean, *Biogeosciences*, 19, 2365–2395 [online]  
1327 Available from: <https://doi.org/10.5194/bg-19-2365-2022>, 2022.
- 1328 Church, M. J., Hutchins, D. A. and Ducklow, H. W.: Limitation of bacterial growth by dissolved  
1329 organic matter and iron in the Southern Ocean, *Appl. Environ. Microbiol.*, 66(2), 455–466,  
1330 doi:10.1128/AEM.66.2.455-466.2000, 2000.
- 1331 Coale, K. H., Johnson, K. S., Fitzwater, S. E., Gordon, R. M., Tanner, S., Chavez, F. P., Ferioli,  
1332 L., Sakamoto, C., Rogers, P., Millero, F., Steinberg, Pa., Nightingale, P., Cooper, D., Cochlan,  
1333 W. P., Landry, M. R., Constantinou, J., Rollwagen, G., Traslavina, A. and Kudela, R.: A massive

- 1334 phytoplankton bloom induced by an ecosystem-scale iron fertilization experiment in the  
1335 equatorial Pacific Ocean, *Nature*, 383(334), 495–501, 1996.
- 1336 Cohen, N. R., McIlvin, M. R., Moran, D. M., Held, N. A., Saunders, J. K., Hawco, N. J.,  
1337 Brosnahan, M., DiTullio, G. R., Lamborg, C., McCrow, J. P., Dupont, C. L., Allen, A. E. and  
1338 Saito, M. A.: Dinoflagellates alter their carbon and nutrient metabolic strategies across  
1339 environmental gradients in the central Pacific Ocean, *Nat. Microbiol.*, 6, 173–186,  
1340 doi:10.1038/s41564-020-00814-7, 2021.
- 1341 Croft, M. T., Lawrence, A. D., Raux-deery, E., Warren, M. J. and Smith, A. G.: Algae acquire  
1342 vitamin B12 through a symbiotic relationship with bacteria, *Nature*, 438, 90–93,  
1343 doi:10.1038/nature04056, 2005.
- 1344 DiTullio, G. and Geesey, M. E.: Photosynthetic Pigments in Marine Algae and Bacteria, in  
1345 *Encyclopedia of Environmental Microbiology*, edited by G. Bitton, pp. 2453–2470, John Wiley  
1346 & Sons, Inc., New York, NY., 2003.
- 1347 DiTullio, G. R., Grebmeier, J. M., Arrigo, K. R. and Lizotte, M. P.: Rapid and early export of  
1348 *Phaeocystis antarctica* blooms in the Ross Sea, *Antarctica, Nature*, 404, 595–598, 2000.
- 1349 DiTullio, G. R. and Smith, W. O. J.: Spatial patterns in phytoplankton biomass and pigment  
1350 distributions in the Ross Sea, *J. Geophys. Res.*, 101, 18467–18477, 1996.
- 1351 DiTullio, G. R., Geesey, M. E., Jones, D. R., Daly, K. L., Campbell, L. and Smith, W. O. J.:  
1352 Phytoplankton assemblage structure and primary productivity along 170° W in the South Pacific  
1353 Ocean, *Mar. Ecol. Prog. Ser.*, 255, 55–80, 2003.
- 1354 DiTullio, G. R., Garcia, N., Riseman, S. F. and Sedwick, P. N.: Effects of iron concentration on  
1355 pigment composition in *Phaeocystis antarctica* grown at low irradiance, *Biogeochemistry*, 83,  
1356 71–81, doi:10.1007/s10533-007-9080-8, 2007.
- 1357 Ducklow, H., Carlson, C., Church, M., Kirchman, D., Smith, D. and Steward, G.: The seasonal  
1358 development of the bacterioplankton bloom in the Ross Sea, *Antarctica, 1994-1997, Deep. Res.*  
1359 *Part II*, 48, 4199–4221, 2001.
- 1360 Ellwood, M. J., Van Den Berg, C. M. G., Boye, M., Veldhuis, M., de Jong, J. T. M., de Baar, H.  
1361 J. W., Croot, P. L. and Kattner, G.: Organic complexation of cobalt across the Antarctic Polar  
1362 Front in the Southern Ocean, *Mar. Freshw. Res.*, 56, 1069–1075, doi:10.1071/MF05097, 2005.
- 1363 Emerson, D.: Biogenic iron dust: A novel approach to ocean iron fertilization as a means of large  
1364 scale removal of carbon dioxide from the atmosphere, *Front. Mar. Sci.*, 6, 22,  
1365 doi:10.3389/fmars.2019.00022, 2019.
- 1366 Fitzwater, S. E., Johnson, K. S., Gordon, R. M., Coale, K. H. and Smith, W. O.: Trace metal  
1367 concentrations in the Ross Sea and their relationship with nutrients and phytoplankton growth,  
1368 *Deep. Res. Part II*, 47, 3159–3179, 2000.
- 1369 Gardner, W. D., Richardson, M. J. and Mishonov, A. V.: Global assessment of benthic nepheloid  
1370 layers and linkage with upper ocean dynamics, *Earth Planet. Sci. Lett.*, 482, 126–134,  
1371 doi:10.1016/j.epsl.2017.11.008, 2018.
- 1372 Glover, D., Jenkins, W. and Doney, S.: *Modeling Methods for Marine Science*, Cambridge  
1373 University Press, New York., 2011.

- 1374 Hawco, N. J., Ohnemus, D. C., Resing, J. A., Twining, B. S. and Saito, M. A.: A dissolved cobalt  
1375 plume in the oxygen minimum zone of the eastern tropical South Pacific, *Biogeosciences*,  
1376 13(20), 5697–5717, doi:10.5194/bg-13-5697-2016, 2016.
- 1377 Hawco, N. J., Lam, P. J., Lee, J., Ohnemus, D. C., Noble, A. E., Wyatt, N. J., Lohan, M. C. and  
1378 Saito, M. A.: Cobalt scavenging in the mesopelagic ocean and its influence on global mass  
1379 balance: Synthesizing water column and sedimentary fluxes, *Mar. Chem.*, (August),  
1380 doi:10.1016/j.marchem.2017.09.001, 2017.
- 1381 Helliwell, K. E.: The roles of B vitamins in phytoplankton nutrition: new perspectives and  
1382 prospects, *New Phytol.*, 216, 62–68, doi:10.1111/nph.14669, 2017.
- 1383 Irving, H. and Williams, R. J. P.: Order of stability of metal complexes, *Nature*, 162, 746–747,  
1384 1948.
- 1385 Jakuba, R. W., Moffett, J. W. and Dyrman, S. T.: Evidence for the linked biogeochemical  
1386 cycling of zinc, cobalt, and phosphorus in the western North Atlantic Ocean, *Global Biogeochem.*  
1387 *Cycles*, 22(4), GB4012, doi:10.1029/2007GB003119, 2008.
- 1388 Jakuba, R. W., Saito, M. A., Moffett, J. W. and Xu, Y.: Dissolved zinc in the subarctic North  
1389 Pacific and Bering Sea: Its distribution, speciation, and importance to primary producers, *Global*  
1390 *Biogeochem. Cycles*, 26, GB2015, doi:10.1029/2010GB004004, 2012.
- 1391 John, S. G., Geis, R. W., Saito, M. A. and Boyle, E. A.: Zinc isotope fractionation during high-  
1392 affinity and low-affinity zinc transport by the marine diatom *Thalassiosira oceanica*, *Limnol.*  
1393 *Oceanogr.*, 52(6), 2710–2714, doi:10.4319/lo.2007.52.6.2710, 2007.
- 1394 Kellogg, R. M.: Assessing the potential for Zn limitation of marine primary production:  
1395 proteomic characterization of the low Zn stress response in marine diatoms, Massachusetts  
1396 Institute of Technology; the Woods Hole Oceanographic Institution., 2022.
- 1397 Kellogg, R. M., McIlvin, M. R., Vedamati, J., Twining, B. S., Moffett, J. W., Marchetti, A.,  
1398 Moran, D. M. and Saito, M. A.: Efficient zinc/cobalt interreplacement in northeast Pacific  
1399 diatoms and relationship to high surface dissolved Co : Zn ratios, *Limnol. Oceanogr.*, 65(11),  
1400 2557–2582, doi:10.1002/lno.11471, 2020.
- 1401 Kellogg, R. M., Moosburner, M. A., Cohen, N. R., Hawco, N. J., McIlvin, M. R., Moran, D. M.,  
1402 DiTullio, G. R., Subhas, A. V., Allen, A. E. and Saito, M. A.: Adaptive responses of marine  
1403 diatoms to zinc scarcity and ecological implications, *Nat. Commun.*, 13, doi:10.1038/s41467-  
1404 022-29603-y, 2022.
- 1405 Kellogg, R. M., Schanke, N. L., Lees, L. E., Chmiel, R. J., Rao, D., Brisbin, M. M., Moran, D.  
1406 M., McIlvin, M. R., Boline, F., Casotti, R., Balestra, C., Horner, T. J., Subhas, A. V., Dunbar,  
1407 R. B., Allen, A. E., DiTullio, G. R. and Saito, M. A.: Zinc co-limitation of natural marine  
1408 phytoplankton assemblages in coastal Antarctica [Submitted].
- 1409 Lane, T. W., Saito, M. A., George, G. N., Pickering, I. J., Prince, R. C. and Morel, F. M. M.: A  
1410 cadmium enzyme from a marine diatom, *Nature*, 435, 42–42,  
1411 doi:https://doi.org/10.1038/435042a, 2005.
- 1412 Lee, J. G. and Morel, F. M. M.: Replacement of zinc by cadmium in marine phytoplankton, *Mar.*  
1413 *Ecol. Prog. Ser.*, 127, 305–309, doi:10.3354/meps127305, 1995.

- 1414 Marsay, C. M., Sedwick, P. N., Dinniman, M. S., Barrett, P. M., Mack, S. L. and McGillicuddy,  
1415 D. J.: Estimating the benthic efflux of dissolved iron on the Ross Sea continental shelf, *Geophys.*  
1416 *Res. Lett.*, 41(21), 7576–7583, doi:10.1002/2014GL061684, 2014.
- 1417 Martin, J. H.: Glacial-interglacial CO<sub>2</sub> change: the iron hypothesis, *Paleoceanography*, 5(1), 1–  
1418 13, doi:https://doi.org/10.1029/PA005i001p00001, 1990.
- 1419 Martin, J. H., Fitzwater, S. E. and Gordon, R. M.: Iron deficiency limits phytoplankton growth in  
1420 Antarctic waters, *Global Biogeochem. Cycles*, 4(1), 5–12, 1990.
- 1421 Mazzotta, M. G., McIlvin, M. R., Moran, D. M., Wang, D. T., Bidle, K. D., Lamborg, C. H. and  
1422 Saito, M. A.: Characterization of the metalloproteome of *Pseudoalteromonas* (BB2-AT2):  
1423 biogeochemical underpinnings for zinc, manganese, cobalt, and nickel cycling in a ubiquitous  
1424 marine heterotroph, *Metallomics*, 13, mfab060, doi:https://doi.org/10.1093/mtomcs/mfab060,  
1425 2021.
- 1426 Monien, D., Monien, P., Brünjes, R., Widmer, T., Kappenberg, A., Silva Busso, A. A.,  
1427 Schnetger, B. and Brumsack, H.-J.: Meltwater as a source of potentially bioavailable iron to  
1428 Antarctica waters, *Antarct. Sci.*, 29(03), 277–291, doi:10.1017/S095410201600064X, 2017.
- 1429 Morel, F. M. M., Reinfeldler, J. R., Roberts, S. B., Chamberlain, C. P., Lee, J. G. and Yee, D.:  
1430 Zinc and carbon co-limitation of marine phytoplankton, *Nature*, 369(6483), 740–742,  
1431 doi:10.1038/369740a0, 1994.
- 1432 Morel, F. M. M., Lam, P. J. and Saito, M. A.: Trace Metal Substitution in Marine Phytoplankton,  
1433 *Annu. Rev. Earth Planet. Sci.*, 48, 491–517, doi:10.1146/annurev-earth-053018-060108, 2020.
- 1434 Noble, A. E., Saito, M. A., Maiti, K. and Benitez-Nelson, C. R.: Cobalt, manganese, and iron  
1435 near the Hawaiian Islands: A potential concentrating mechanism for cobalt within a cyclonic  
1436 eddy and implications for the hybrid-type trace metals, *Deep. Res. Part II Top. Stud. Oceanogr.*,  
1437 55(10–13), 1473–1490, doi:10.1016/j.dsr2.2008.02.010, 2008.
- 1438 Noble, A. E., Moran, D. M., Allen, A. E. and Saito, M. A.: Dissolved and particulate trace metal  
1439 micronutrients under the McMurdo Sound seasonal sea ice: basal sea ice communities as a  
1440 capacitor for iron, *Front. Chem.*, 1, 25, doi:10.3389/fchem.2013.00025, 2013.
- 1441 Noble, A. E., Ohnemus, D. C., Hawco, N. J., Lam, P. J. and Saito, M. A.: Coastal sources, sinks  
1442 and strong organic complexation of dissolved cobalt within the US North Atlantic GEOTRACES  
1443 transect GA03, *Biogeosciences*, 14(11), 2715–2739, doi:10.5194/bg-14-2715-2017, 2017.
- 1444 Oldham, V. E., Chmiel, R., Hansel, C. M., DiTullio, G. R., Rao, D. and Saito, M.: Inhibited  
1445 manganese oxide formation hinders cobalt scavenging in the Ross Sea, *Global Biogeochem.*  
1446 *Cycles*, 35, e2020GB006706, doi:10.1029/2020GB006706, 2021.
- 1447 Osman, D., Cooke, A., Young, T. R., Deery, E., Robinson, N. J. and Warren, M. J.: The  
1448 requirement for cobalt in vitamin B12: A paradigm for protein metalation, *Biochim. Biophys.*  
1449 *Acta - Mol. Cell Res.*, 1868, 118896, doi:10.1016/j.bbamcr.2020.118896, 2021.
- 1450 Peloquin, J. A. and Smith, W. O. J.: Phytoplankton blooms in the Ross Sea, Antarctica:  
1451 Interannual variability in magnitude, temporal patterns, and composition, *J. Geophys. Res.*, 112,  
1452 C08013, doi:10.1029/2006JC003816, 2007.



- 1453 Planquette, H., Sherrell, R. M., Stammerjohn, S. and Field, M. P.: Particulate iron delivery to the  
1454 water column of the Amundsen Sea, Antarctica, *Mar. Chem.*, 153, 15–30,  
1455 doi:10.1016/j.marchem.2013.04.006, 2013.
- 1456 Price, N. M., Harrison, G. I., Hering, J. G., Hudson, R. J., Pascale, M., Nirel, V., Palenik, B. and  
1457 Morel, F. M. M.: Preparation and Chemistry of the Artificial Algal Culture Medium Aquil, *Biol.*  
1458 *Oceanogr.*, 6, 443–461, 2013.
- 1459 Rao, D.: Characterizing cobalamin cycling by Antarctic marine microbes across multiple scales,  
1460 Massachusetts Institute of Technology; the Woods Hole Oceanographic Institution., 2020.
- 1461 Rao, D., Fussy, Z., Moran, D. M., McIlvin, M. R., Allen, A. E., Follows, M. J. and Saito, M. A.:  
1462 Flexible B12 ecophysiology of *Phaeocystis antarctica* to a fusion B12-independent methionine  
1463 synthase with widespread homologues [In review]., *PNAS* [online] Available from:  
1464 <http://arxiv.org/abs/1712.09707>.
- 1465 Roberts, S. B., Lane, T. W. and Morel, F. M. M.: Carbonic Anhydrase in the Marine Diatom  
1466 *Thalassiosira weissflogii* (Bacillariophyceae), *J. Phycol.*, 33(5), 845–850, doi:10.1111/j.0022-  
1467 3646.1997.00845.x, 1997.
- 1468 Rodionov, D. A., Vitreschak, A. G., Mironov, A. A. and Gelfand, M. S.: Comparative genomics  
1469 of the vitamin B12 metabolism and regulation in prokaryotes, *J. Biol. Chem.*, 278(42), 41148–  
1470 41159, doi:10.1074/jbc.M305837200, 2003.
- 1471 Rose, J. M., Feng, Y., DiTullio, G. R., Dunbar, R. B., Hare, C. E., Lee, P. A., Lohan, M., Long,  
1472 M., Smith, W. O., Sohst, B., Tozzi, S., Zhang, Y. and Hutchins, D. A.: Synergistic effects of iron  
1473 and temperature on Antarctic phytoplankton and microzooplankton assemblages,  
1474 *Biogeosciences*, 6, 3131–3147, doi:10.5194/bg-6-3131-2009, 2009.
- 1475 Saito, M. A. and Goepfert, T. J.: Zinc-cobalt colimitation of *Phaeocystis antarctica*, *Limnol.*  
1476 *Oceanogr.*, 53(1), 266–275, 2008.
- 1477 Saito, M. A. and Moffett, J. W.: Complexation of cobalt by natural organic ligands in the  
1478 Sargasso Sea as determined by a new high-sensitivity electrochemical cobalt speciation method  
1479 suitable for open ocean work, *Mar. Chem.*, 75(1–2), 49–68, doi:10.1016/S0304-4203(01)00025-  
1480 1, 2001.
- 1481 Saito, M. A., Rocap, G. and Moffett, J. W.: Production of cobalt binding ligands in a  
1482 *Synechococcus* feature at the Costa Rica upwelling dome, *Limnol. Oceanogr.*, 50(1), 279–290,  
1483 2005.
- 1484 Saito, M. A., Goepfert, T. J., Noble, A. E., Bertrand, E. M., Sedwick, P. N. and DiTullio, G. R.:  
1485 A seasonal study of dissolved cobalt in the Ross Sea, Antarctica: micronutrient behavior,  
1486 absence of scavenging, and relationships with Zn, Cd, and P, *Biogeosciences*, 7, 4059–4082,  
1487 doi:10.5194/bg-7-4059-2010, 2010.
- 1488 Saito, M. A., Noble, A. E., Hawco, N., Twining, B. S., Ohnemus, D. C., John, S. G., Lam, P.,  
1489 Conway, T. M., Johnson, R., Moran, D. and McIlvin, M.: The acceleration of dissolved cobalt's  
1490 ecological stoichiometry due to biological uptake, remineralization, and scavenging in the  
1491 Atlantic Ocean, *Biogeosciences*, 14(20), 4637–4662, doi:10.5194/bg-14-4637-2017, 2017.

- 1492 Sañudo-Wilhelmy, S. A., Gobler, C. J., Okbami, M. and Taylor, G. T.: Regulation of  
1493 phytoplankton dynamics by vitamin B12, *Geophys. Res. Lett.*, 33(4), 10–13,  
1494 doi:10.1029/2005GL025046, 2006.
- 1495 Sedwick, P. N. and DiTullio, G. R.: Regulation of algal blooms in Antarctic shelf waters by the  
1496 release of iron from melting sea ice, *Geophys. Res. Lett.*, 24(20), 2515–2518, 1997.
- 1497 Sedwick, P. N., DiTullio, G. R. and Mackey, D. J.: Iron and manganese in the Ross Sea,  
1498 Antarctica: Seasonal iron limitation in Antarctic shelf waters, *J. Geophys. Res.*, 105(C5), 11321–  
1499 11336, 2000.
- 1500 Sedwick, P. N., Marsay, C. M., Sohst, B. M., Aguilar-Islas, A. M., Lohan, M. C., Long, M. C.,  
1501 Arrigo, K. R., Dunbar, R. B., Saito, M. A., Smith, W. O. and DiTullio, G. R.: Early season  
1502 depletion of dissolved iron in the Ross Sea polynya: Implications for iron dynamics on the  
1503 Antarctic continental shelf, *J. Geophys. Res.*, 116, C12019, doi:10.1029/2010JC006553, 2011.
- 1504 Smetacek, V., Klaas, C., Strass, V. H., Assmy, P., Montresor, M., Cisewski, B., Savoye, N.,  
1505 Webb, A., D'Ovidio, F., Arrieta, J. M., Bathmann, U., Bellerby, R., Berg, G. M., Croot, P.,  
1506 Gonzalez, S., Henjes, J., Herndl, G. J., Hoffmann, L. J., Leach, H., Losch, M., Mills, M. M.,  
1507 Neill, C., Peeken, I., Röttgers, R., Sachs, O., Sauter, E., Schmidt, M. M., Schwarz, J.,  
1508 Terbrüggen, A. and Wolf-Gladrow, D.: Deep carbon export from a Southern Ocean iron-  
1509 fertilized diatom bloom, *Nature*, 487, 313–319, doi:10.1038/nature11229, 2012.
- 1510 Smith, W. O. J. and Jones, R. M.: Vertical mixing, critical depths, and phytoplankton growth in  
1511 the Ross Sea, *ICES J. Mar. Sci.*, 72(6), 1952–1960, 2015.
- 1512 Spackeen, J. L., Sipler, R. E., Bertrand, E. M., Xu, K., McQuaid, J. B., Walworth, N. G.,  
1513 Hutchins, D. A., Allen, A. E. and Bronk, D. A.: Impact of temperature, CO<sub>2</sub>, and iron on nutrient  
1514 uptake by a late-season microbial community from the Ross Sea, Antarctica, *Aquat. Microb.  
1515 Ecol.*, 82, 145–159, doi:10.3354/ame01886, 2018.
- 1516 St-Laurent, P., Yager, P. L., Sherrell, R. M., Stammerjohn, S. E. and Dinniman, M. S.: Pathways  
1517 and supply of dissolved iron in the Amundsen Sea (Antarctica), *J. Geophys. Res. Ocean.*, 122(9),  
1518 7135–7162, doi:10.1002/2017JC013162, Received, 2017.
- 1519 Sunda, W. G.: Trace metal interactions with marine phytoplankton, *Biol. Oceanogr.*, 6(5–6),  
1520 411–442, doi:10.1080/01965581.1988.10749543, 1989.
- 1521 Sunda, W. G.: Feedback interactions between trace metal nutrients and phytoplankton in the  
1522 ocean, *Front. Microbiol.*, 3, 204, doi:10.3389/fmicb.2012.00204, 2012.
- 1523 Sunda, W. G. and Huntsman, S. A.: Regulation of cellular manganese and manganese transport  
1524 in the unicellular alga *Chlamydomonas*, *Limnol. Oceanogr.*, 30(1), 71–80,  
1525 doi:10.4319/lo.1985.30.1.0071, 1985.
- 1526 Sunda, W. G. and Huntsman, S. A.: Feedback interactions between zinc and phytoplankton in  
1527 seawater, *Limnol. Oceanogr.*, 37(1), 25–40, doi:10.4319/lo.1992.37.1.0025, 1992.
- 1528 Sunda, W. G. and Huntsman, S. A.: Cobalt and zinc interreplacement in marine phytoplankton:  
1529 Biological and geochemical implications, *Limnol. Oceanogr.*, 40(8), 1404–1417,  
1530 doi:10.4319/lo.1995.40.8.1404, 1995.
- 1531 Sunda, W. G. and Huntsman, S. A.: Antagonisms between cadmium and zinc toxicity and  
1532 manganese limitation in a coastal diatom, *Limnol. Oceanogr.*, 41(3), 373–387, 1996.

- 1533 Sunda, W. G. and Huntsman, S. A.: Effect of Zn, Mn, and Fe on Cd accumulation in  
1534 phytoplankton: Implications for oceanic Cd cycling, *Limnol. Oceanogr.*, 45(7), 1501–1516,  
1535 2000.
- 1536 Taylor, G. T. and Sullivan, C. W.: Vitamin B12 and cobalt cycling among diatoms and bacteria  
1537 in Antarctic sea ice microbial communities, *Limnol. Oceanogr.*, 53(5), 1862–1877, 2008.
- 1538 Warren, M. J., Raux, E., Schubert, H. L. and Escalante-Semerena, J. C.: The biosynthesis of  
1539 adenosylcobalamin (vitamin B12), *Nat. Prod. Rep.*, 19, 390–412, doi:10.1039/B108967F, 2002.
- 1540 Westerlund, S. and Öhman, P.: Cadmium, copper, cobalt, nickel, lead, and zinc in the water  
1541 column of the Weddell Sea, Antarctica, *Geochim. Cosmochim. Acta*, 55(8), 2127–2146,  
1542 doi:10.1016/0016-7037(91)90092-J, 1991.
- 1543 Zhu, Z., Xu, K., Fu, F., Spackeen, J. L., Bronk, D. A. and Hutchins, D. A.: A comparative study  
1544 of iron and temperature interactive effects on diatoms and *Phaeocystis antarctica* from the Ross  
1545 Sea, Antarctica, *Mar. Ecol. Prog. Ser.*, 550, 39–51, doi:10.3354/meps11732, 2016.